Palaeogeography, Palaeoclimatology, Palaeoecology 676 (2025) 113164

Contents lists available at ScienceDirect

Palaeogeography, Palaeoclimatology, Palaeoecology

journal homepage: www.elsevier.com/locate/palaeo

Opening of South China Sea in the Western Pacific forcing the climate cooling and lake level rise at Eocene–Oligocene transition

Jing Guo [a,b], Fujie Jiang [a,b,*], Guangrong Peng [c,d], Yuqi Wu [a,b], Weibing Shen [a,b], Rui Zhang [a,b], Yu An [e], Dapeng Jiang [c,d], Fusheng Yu [a,b], Yaqi Li [a,b], Zhifeng Yu [a,b], Jiabing Jiang [a,b]

[a] National Key Laboratory of Petroleum Resources and Engineering, China University of Petroleum, Beijing 102249, China
[b] College of Geosciences, China University of Petroleum, Beijing 102249, China
[c] Shenzhen Branch, CNOOC Ltd., Shenzhen, Guangdong 518054, China
[d] China National Offshore Oil Corporation Deepwater Development Ltd, Shenzhen, Guangdong 518054, China
[e] College of Resources and Environmental Engineering, Inner Mongolia university of technology, Hohhot 010051, China

ARTICLE INFO

Editor: M Elliot

Keywords:
Eocene–Oligocene transition
Climate cooling
Terrestrial response
Tectonic reorganization
South China Sea

ABSTRACT

The Eocene–Oligocene transition (EOT, 33.9 Ma) marks a major global climate shift from greenhouse to icehouse conditions. However, the spatial heterogeneity of terrestrial responses to climate transitions and tectonic mechanisms driving this global cooling remain poorly understood. This study presents terrestrial records from the Pearl River Mouth Basin (PRMB) in the South China Sea (SCS) that span the Late Eocene to Early Oligocene. Using data on total organic carbon (TOC) content, elemental geochemistry, and carbonate carbon ($\delta^{13}C_{carb}$) and oxygen ($\delta^{18}O_{carb}$) isotopes, we identified the 33.9 Ma EOT at the boundary between the Enping and Zhuhai formations in the PRMB. The results revealed a significant reduction in weathering, temperature, and precipitation in the SCS during the EOT, synchronous with global cooling. Notably, the mudstone strata and increased Mn/(Fe + Ti) ratio at the base of Zhuhai Formation indicate a sudden lake-level rise at 33.9 Ma, in contrast to the global sea-level decline. The tectonic evolution of the SCS has driven regional cooling and hydrological changes. We found that the TOC peak, along with positive $\delta^{13}C_{carb}$ and $\delta^{18}O_{carb}$ excursions, corresponds with the opening of the SCS, leading to decreased pCO_2 levels. This tectonically driven carbon feedback mechanism, along with the reorganization of ocean currents, enhanced productivity, sequestered atmospheric CO_2, and drove global cooling. The observed lake-level rise in the PRMB has also been attributed to Pacific seawater transgression after the opening of the SCS. This study provides insights into the relationship between regional and global climate dynamics, which will guide future climate change research.

1. Introduction

The Eocene–Oligocene Transition (EOT, ~34 Ma) marks a critical shift from a greenhouse to an icehouse (Miller et al., 1987; Zachos et al., 2001, 2008; Liu et al., 2009), leading to notable global climate changes. This transition is characterized by a marked drop in global temperatures (Pagani et al., 2005; Pearson et al., 2009), a reduction in atmospheric pCO_2 levels (Coxall et al., 2005), and expansion of the Antarctic ice sheet (Zachos et al., 2001; Miller et al., 2020). Marine records, such as changes in $\delta^{13}C$ and $\delta^{18}O$ values, indicate widespread cooling, along with a sea level decline of 55–70 m. Ocean circulation also underwent reorganization (Zachos and Kump, 2005; Liu et al., 2018), with increased primary productivity and the turnover of benthic foraminifera (e.g., Egan et al., 2013; Houben et al., 2013; Villa et al., 2014; López-Quirós et al., 2021). The likely causes of this transition include tectonic reorganization (Kennett et al., 1974; Shackleton and Kennett, 1975; Raymo and Ruddiman, 1992), reduction in atmospheric pCO_2 levels (DeConto and Pollard, 2003; Colwyn and Hren, 2019), the global carbon cycle (Zachos and Kump, 2005; Tigchelaar et al., 2011; Zhang et al., 2011; Herman et al., 2013), orbital forcing (Zachos et al., 2001; Ao et al., 2020), meteorite impacts (Vonhof et al., 2000), and volcanic eruptions (Jicha et al., 2009).

Research on the EOT has largely focused on marine records, with studies spanning the equatorial Pacific (Coxall et al., 2005; Coxall et al.,

* Corresponding author at: National Key Laboratory of Petroleum Resources and Engineering, China University of Petroleum, Beijing 102249, China.
E-mail address: jfjhtb@163.com (F. Jiang).

https://doi.org/10.1016/j.palaeo.2025.113164
Received 7 April 2025; Received in revised form 18 July 2025; Accepted 21 July 2025
Available online 23 July 2025

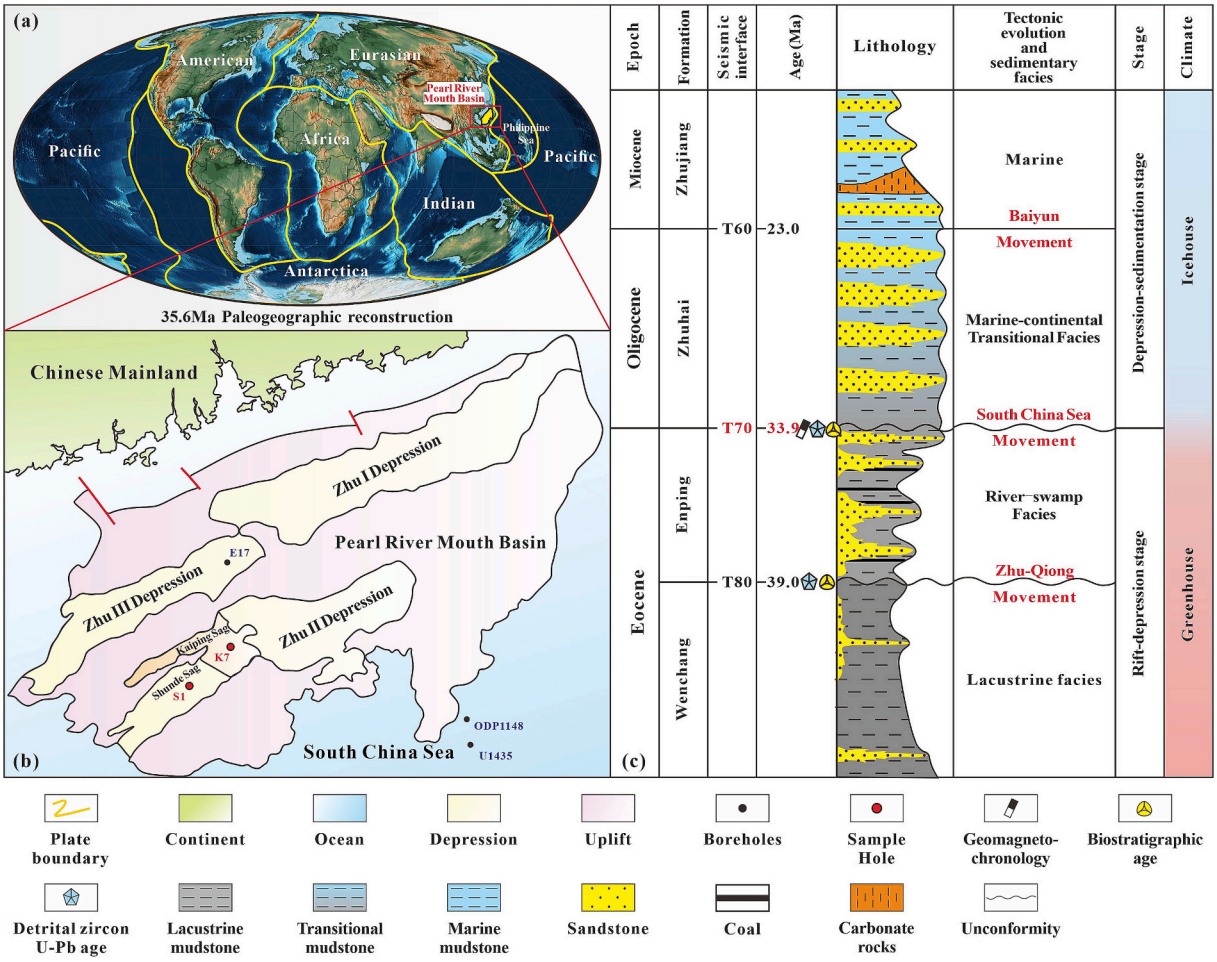

Fig. 1. (a) Paleogeographic evolution of Paleogene of 35.6 Ma, global Plate distribution and the location of PRMB (Modified from Scotese, 2014; Ma et al., 2020); (b) The location and tectonic division of the PRMB and location of sampling well (Modified from Peng et al., 2023); (c) Stratigraphic characteristics of Kaiping Sag, PRMB. Stratigraphy, seismic interface, age, lithology, tectonic evolution, sedimentary facies, and climatic evolution of the Kaiping Sag since the Eocene are described (Modified from Zhang et al., 2020).

2011), southern Indian Ocean (Zachos et al., 1992), and South Atlantic (Lear et al., 2008; Pearson et al., 2008; Katz et al., 2008; Miller et al., 2008). These studies highlight a drop in global temperatures, expansion of the Antarctic ice sheet, and a drastic decrease in atmospheric pCO_2 levels. Conversely, terrestrial records show substantial regional variabilities (Pound and Salzmann, 2017). For example, while East Asian experienced an increased seasonal precipitation (Sun and Windley, 2015), the Central Asian interior showed intensified aridification (Bosboom et al., 2014). The Tibetan Plateau recorded a reduction in continental weathering (Sun et al., 2022; Tang et al., 2024), whereas the Mongolian Gobi deserts exhibited enhanced weathering (Wang et al., 2023a). The heterogeneity of climate responses in terrestrial basins remains a key challenge, particularly as the mechanisms behind these diverse climate responses remain largely unclear.

In this study, we address the gap in understanding the impact of the EOT on the western Pacific, specifically the South China Sea (SCS). We focused on the Pearl River Mouth Basin (PRMB), which underwent notable tectonic rifting and environmental transitions (Wu et al., 2016; 2018) coinciding with global climate cooling during the EOT. Total organic carbon (TOC), elemental, and isotope geochemical analyses were conducted to reconstruct the paleoclimate and water environment of the PRMB. Our findings link the opening of the SCS to a reduction in atmospheric pCO_2 levels, providing insights into the role of tectonic movements in regional climate change. This study offers a key perspective on the spatial heterogeneity of EOT climate responses and enhances our understanding of tectonic-climate coupling in the western Pacific.

2. Geological setting

Pearl River Mouth Basin in the SCS is situated at the tectonic intersection of the Eurasian, Pacific, and Indo–Australian plates (Peng et al., 2023; Gao et al., 2024; Fig. 1a). Throughout the Cenozoic, the basin has undergone multiple tectonic events, with previous studies identifying regional unconformities resulting from tectonic movements, including the Zhu-Qiong, SCS, and Baiyun movements (Fig. 1c, Ru, 1988; Li, 1993; Mi et al., 2008). The SCS movement marks the transition of the basin from a rifting to a depression and sedimentation stages, resulting in the formation of the T70 unconformity surface (Zhang et al., 2018). Below the T70 unconformity, Eocene terrestrial deposits, such as the Wenchang and Enping formations, were laid down, whereas marine strata, including the Zhuhai formation and overlying strata, were deposited above it (Fig. 1c, Mi et al., 2008; Gao et al., 2023).

The Enping Formation is characterized by river delta and swamp depositional environments, with interbedded sandstone and mudstone containing abundant carbonized plant debris and coal seams (Pang et al., 2018; Zhang et al., 2020). Conversely, the Zhuhai Formation represents a transition from terrestrial to marine environments, comprising interbedded sandstone and mudstone, with thin limestone layers. Based on deep magnetic data (Li et al., 2014), microfossils study (Li et al., 2016), U—Pb zircon dating (Shao et al., 2017), and palynological assemblages data (Zhang et al., 2020), the boundary between the

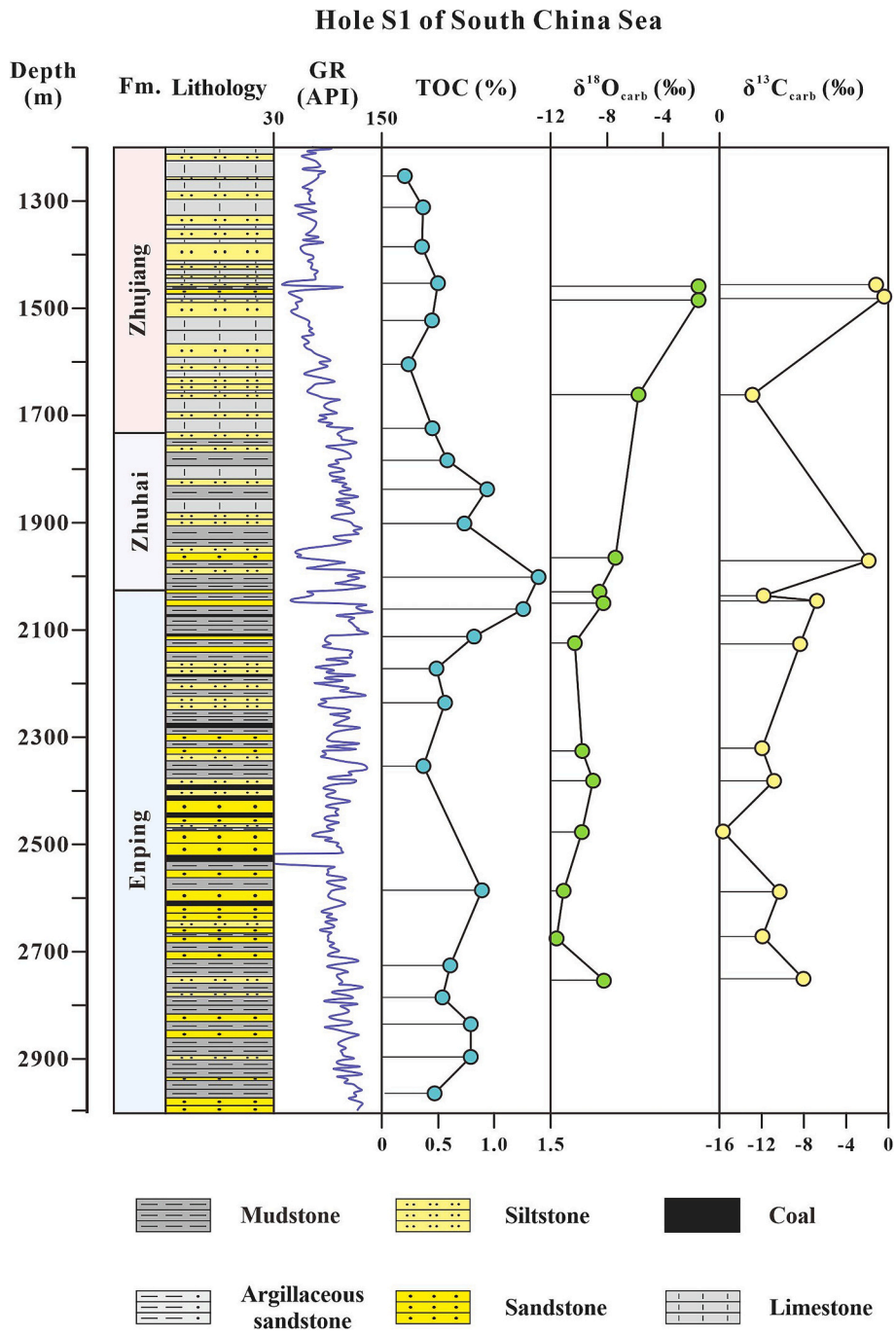

Fig. 2. Sampling depth, TOC content, $\delta^{13}C_{carb}$, and $\delta^{18}C_{carb}$ from Hole S1 in the PRMB.

Enping and Zhuhai formations in the PRMB was dated to 33.9 Ma (Fig. 1c). This boundary aligns with the global transition from a greenhouse to an icehouse climate (Zhang et al., 2020).

3. Materials and methods

3.1. Samples and experiments

In this study, samples were collected from Hole S1 of the Shunde Sag and Hole K7 of the Kaiping Sag in the PRMB, SCS (Fig. 1b), from archived cores. A total of 22 mudstone samples from Hole S1 were analyzed for TOC, while 13 samples were analyzed for carbonate carbon ($\delta^{13}C_{carb}$) and oxygen ($\delta^{18}O_{carb}$) isotopes (Fig. 2, 5e). In addition, 47 mudstone samples from Hole K7 were analyzed for elemental geochemistry (Fig. 3, 5d). Some samples from Hole K7 were subjected to vitrinite reflectance (R_o) measurements. These selected samples span the Eocene–Oligocene boundary, making them ideal for recording the EOT events.

3.1.1. TOC analysis

The TOC content was determined using a LECO CS-230 carbon-sulfur analyzer. The samples were first ground to a particle size of less than 200 mesh. Inorganic carbon was removed by treatment with hydrochloric acid, followed by rinsing with distilled water for neutralization. The organic carbon in the samples was then combusted to CO_2 in a high-temperature furnace with a catalyst at 900–950 °C. The CO_2 content was measured using nondispersive infrared absorption. The TOC value was calculated based on the established relationship between CO_2 and

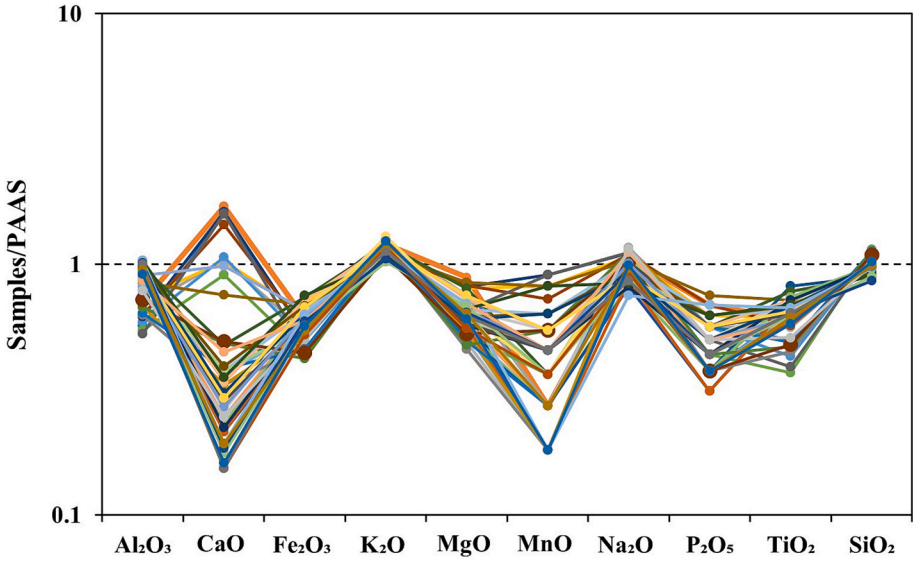

Fig. 3. Distribution patterns of the analyzed samples for major oxides (PAAS-normalized).

TOC contents (Farhaduzzaman et al., 2012).

3.1.2. $\delta^{13}C_{carb}$ and $\delta^{18}O_{carb}$ analysis

For the analysis of $\delta^{13}C_{carb}$ and $\delta^{18}O_{carb}$, powdered 200 mesh samples were placed in a reaction vessel and treated with 100 % anhydrous phosphoric acid. The vessel was evacuated and heated for 30 min to remove moisture from the samples. The carbonate reacted with phosphoric acid at 70 °C, releasing CO_2, which then passed through a gas chromatography column to separate it from other impurity gases. The collected CO_2 gas was analyzed for carbon and oxygen isotopes using a Delta V Advantage isotope-ratio mass spectrometer with a dual-inlet system. The $\delta^{13}C_{carb}$ and $\delta^{18}O_{carb}$ values were calculated relative to the Peedee Belemnite (PDB) standard (National Energy Administration, China, 2019).

3.1.3. Elemental geochemical analysis

An inductively coupled plasma-mass spectrometry (ICP-MS) was used to determine the major elemental content, using SY/T 6404–2018 elemental analysis execution standards (National Energy Administration, China, 2018). The sample was crushed to a particle size of less than 74 μm. The sample was placed in a vessel, 5–10 mL of a mixture of hydrofluoric acid, nitric acid, and perchloric acid was added, and pretreated according to a programmed temperature profile. After cooling, the excess acid was evaporated and diluted. The sample was introduced into the ICP-MS, the element concentrations were calculated based on the calibration curve, and mass bias correction was performed. The results of the measurements included the contents of Al_2O_3, CaO, Fe_2O_3, K_2O, MgO, MnO, Na_2O, P_2O_5, TiO_2, and SiO_2.

3.1.4. Vitrinite reflectance (R_o) analysis

The samples were sliced and polished into thin sections and placed in a drying chamber for 12 h. After drying, a drop of immersion oil was applied to the prepared sample and observed under a Leica polarizing microscope. Reflectance measurements were conducted using a light source with a wavelength of 546 ± 5 nm. The reflectance of the samples was determined by comparing their reflectance intensities with those of a standard reference slide with known reflectivity (National Energy Administration, China, 2012). Multiple measurements of the reflectance intensity were taken at the same measurement point, and the average reflectance value was calculated as the final result.

3.2. Methods for reconstructing paleoenvironments

3.2.1. The calculation of chemical weathering proxies

Fine-grained sedimentary rocks can record the weathering of the source area. The ratios of active and inert elements, including the chemical index of alteration (CIA, Nesbitt and Young, 1982, 1984), plagioclase index of alteration (PIA, Fedo et al., 1995; Nesbitt and Young, 1982), and chemical index of weathering (CIW, Harnois, 1988), are widely used for the quantitative evaluation of chemical weathering intensity. CIA, PIA, and CIW were calculated using the following formula based on the main elemental contents:

$$CIA = Al_2O_3/(Al_2O_3 + K_2O + Na_2O + CaO^*) \times 100 \quad (1)$$

$$PIA = [Al_2O_3 - K_2O)/(Al_2O_3 + Na_2O + CaO^* - K_2O)] \times 100 \quad (2)$$

$$CIW = Al_2O_3/(Al_2O_3 + Na_2O + CaO^*) \times 100 \quad (3)$$

CaO* represents CaO in silicate minerals. Due to the lack of data on carbon dioxide, it was not possible to correct for the carbonate fractions (Fedo et al., 1995). Therefore, we adopted the following assumption: when $CaO < Na_2O$, $CaO^* = CaO$; when $CaO > Na_2O$, $CaO^* = Na_2O$ is used to correct for the calcium oxide content (Nesbitt and Young, 1982). In the process of chemical weathering, the loss of unstable cations (such as Ca^{2+}, Na^+, and K^+) and the retention of stable cations (such as Al^{3+} and Ti^{4+}) can easily form a warm and humid climate. In contrast, lower weather proxies indicate a lack of or negligible chemical weathering, reshaping the cold and arid climate. Specifically, CIA values of 50–60, 60–80, and 80–100 represent weak weathering, moderate weathering, and intense weathering under cold and dry to warm and humid conditions, respectively (Fedo et al., 1995).

3.2.2. The calculation of paleoprecipitation and paleotemperature proxies

Sheldon et al. (2002) determined the estimation formulas for paleoprecipitation and paleotemperature based on changes in major elements and climate data from North American soil (Sheldon et al., 2002; Retallack, 2001, Retallack, 2000; Maynard, 1992). Paleoprecipitation proxies are applicable to the precipitation range of 200–1600 mm/year, whereas paleotemperature proxies are suitable for predicting high temperatures of 8–22 °C (Sheldon et al., 2002). The estimation formulas are as follows:

$$MAPa = 221\ e^{0.0197CIW} \quad (4)$$

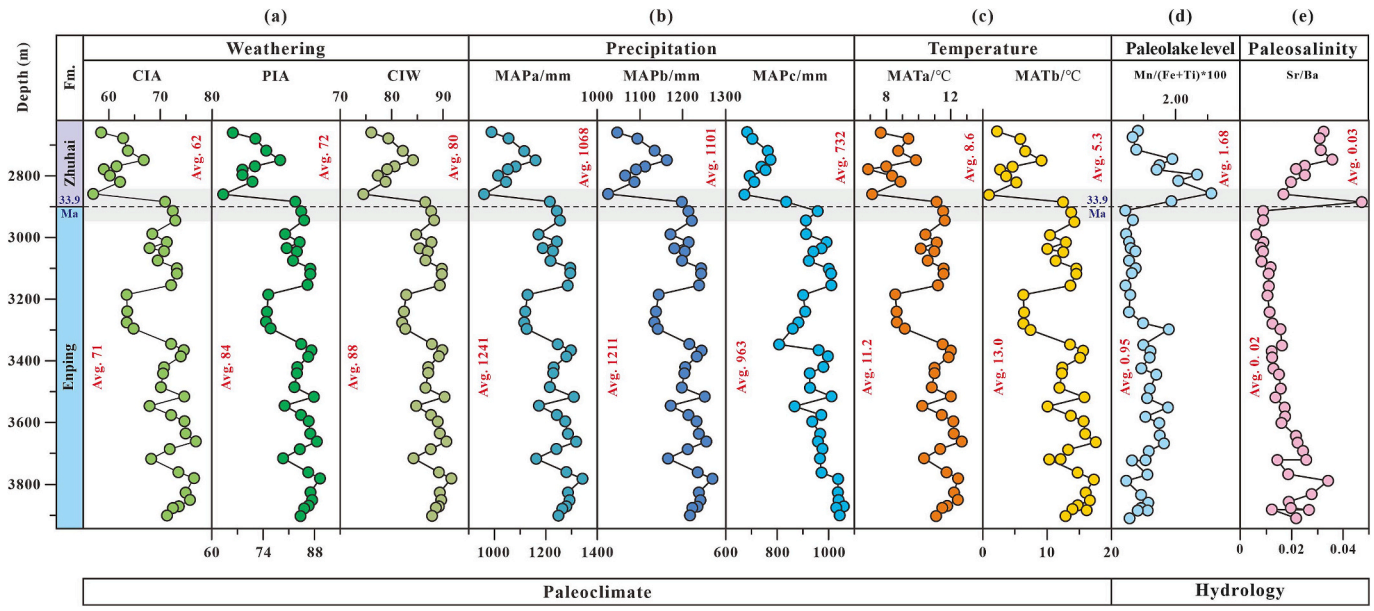

Fig. 4. Reconstructions of the (a) weathering, (b) Mean Annual Precipitation (MAP), (c) Mean Annual Temperature (MAT), (d) Paleo lake-level, and (e) Paleosalinity of the PRMB from Eocene to Oligocene. At 33.9 Ma, the boundary between the Enping and Zhuhai formations, there was a sudden decrease in weathering, MAP, and MAT, indicating that the SCS also experienced cooling during the EOT. A rise in lake level and increase in salinity indicate the SCS experienced Hydrological changes during the EOT.

$$MAPb = 14.26\ CIW - 37.632 \quad (5)$$

$$MAPc = -130.93 \ln(CaO/Al_2O_3) + 467.4 \quad (6)$$

$$MATa = -18.516([Na_2O + K_2O]/Al_2O_3) + 17.298 \quad (7)$$

Applying these formulas to the Eocene and Oligocene paleosol sequences in central Oregon, refined paleoprecipitation and paleotemperature estimates consistent with other pedogenic and paleobotanical transfer functions were obtained (Sheldon et al., 2002). Precipitation and temperature proxies are sufficiently robust to be applied to most paleosoils; however, their applicability to soils in swamps, deserts, or deeply weathered tropical regions is not unlimited (Sheldon et al., 2002). The temperature sensitivity recorded by the CIA in Southeast Asia (approximately 0.8 CIA units/°C) is consistent with observations of modern surface soils and river sediments (Li et al., 2022). In contrast, weathering intensity in East Asia is more sensitive to temperature changes. Based on this, a fitting formula for the CIA and MAT of river sediments in East Asia was established:

$$MATb = (CIA - 55.8)/1.2 \quad (8)$$

This method has been widely applied to paleoclimate reconstruction of terrestrial sediments (Li et al., 2024b; Wu et al., 2025).

3.2.3. *The calculation of paleolake level and paleosalinity proxies*

To reconstruct changes in paleolake levels, this study comprehensively utilized gamma ray (GR) curves, stratigraphic lithology analysis, and geochemical proxies. The GR curve reflects the content of radioactive elements such as uranium (U), thorium (Th), and potassium (K) within the formation (Ruffell and Worden, 2000). Typically, shale and mudstone exhibit higher GR values, whereas sandstone and carbonate rocks have lower GR values. In lake sedimentary environments, areas with high GR values often indicate deeper lake basins, as these areas have weaker hydrodynamic conditions, making it easier for fine-grained materials to settle (Miall, 1996).

Additionally, the lithology of the strata is an important indicator of paleolake levels. Mudstone and shale are typically deposited in deeper lake environments, whereas sandstone and carbonate rocks are more commonly found at shallower lake edges or in deltaic settings (Miall, 1996).

In both marine and terrestrial sedimentary systems, the differential geochemical behavior of iron (Fe) and titanium (Ti) compared to manganese (Mn) creates distinct spatial distribution patterns. Fe and Ti are more mobile during early diagenesis, leading to their enrichment in proximal settings, whereas Mn is relatively stable and tends to accumulate in distal basin environments (Rieu et al., 2007; Naeher et al., 2013). The establishment of stable water column stratification combined with basin circulation dynamics induces predictable variations in the Mn/(Fe + Ti) ratios, rendering this geochemical proxy particularly effective for water level reconstruction. Elevated Mn/(Fe + Ti) values correspond to deeper water levels, as documented in both marine and terrestrial systems (Tribovillard et al., 2006; Wu et al., 2024).

The Sr/Ba ratio serves as a sensitive proxy for salinity fluctuations in aqueous environments and shows a positive correlation with paleosalinity estimates derived from sedimentary records (Wei and Algeo, 2020).

4. Results

4.1. *TOC, $\delta^{13}C_{carb}$, $\delta^{18}C_{carb}$ and elemental characteristics*

TOC content serves as a parameter for assessing the paleoproductivity of terrestrial systems. The TOC content of 22 mudstone samples from Hole S1 ranged from 0.21 to 1.39 wt% (avg. 0.63 wt%), with a peak of 1.39 wt% recorded at the boundary between the Enping and Zhuhai Formations (Fig. 2), indicative of enhanced primary productivity during this depositional interval.

$\delta^{13}C_{carb}$ and $\delta^{18}O_{carb}$ provide crucial constraints on paleoclimatic and paleoenvironmental conditions (Lettéron et al., 2017). The results show $\delta^{13}C_{carb}$ values ranging from −15.73 ‰ to −0.50 ‰ (avg. −8.65 ‰) and $\delta^{18}O_{carb}$ values from −11.63 ‰ to −1.50 ‰ (avg. −7.90 ‰). Notably, both isotopic proxies exhibited marked positive excursions at the boundary between the Enping and Zhuhai Formations (Fig. 2), recording significant climatic perturbations in the SCS during this stratigraphic interval.

Elemental analysis of 47 mudstone samples from Hole K7 revealed distinct geochemical variations in the elemental oxide composition

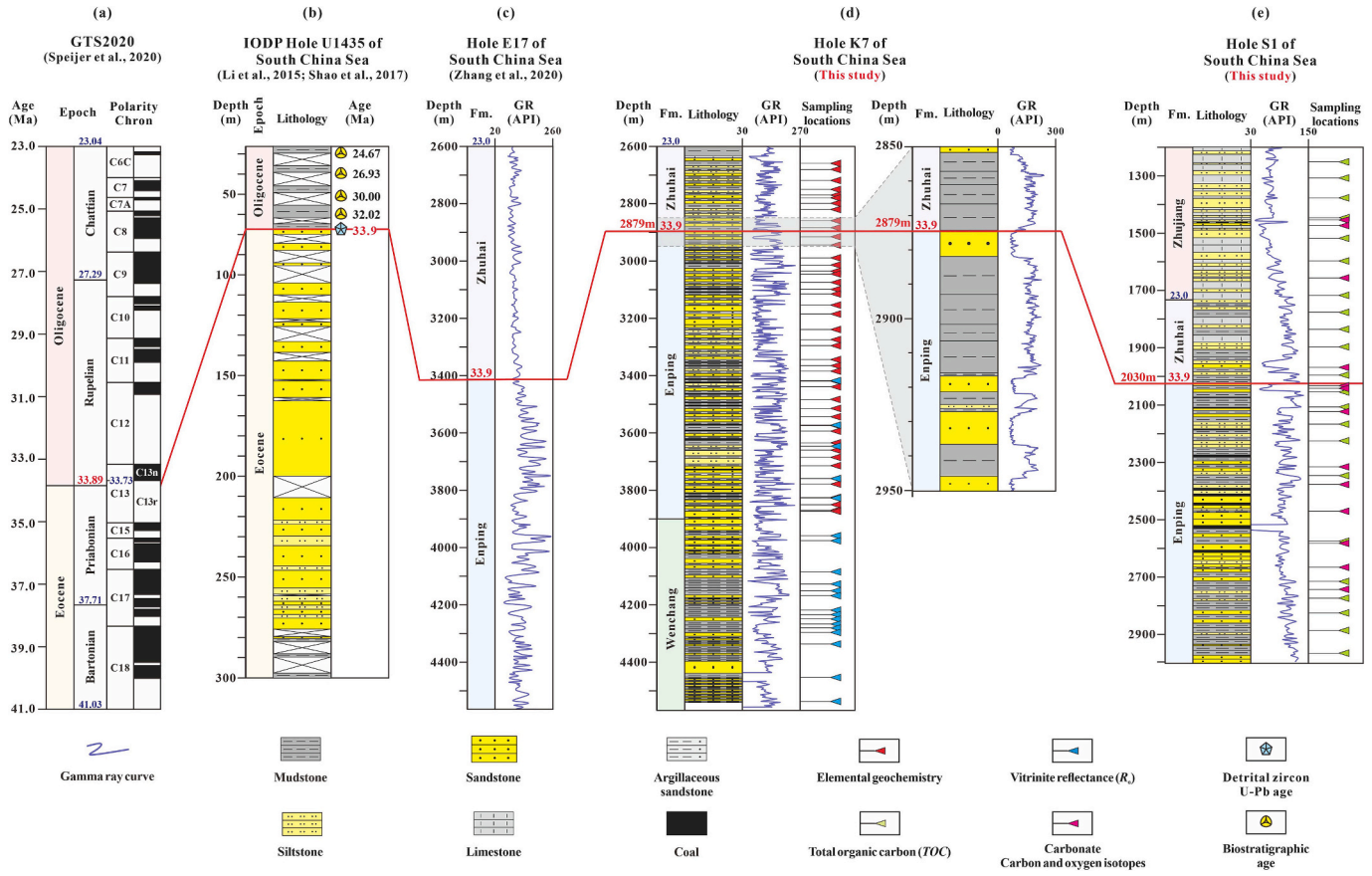

Fig. 5. Age model of Eocene and Oligocene strata of the SCS. (a) The age model of GTS2020 (Speijer et al., 2020); the boundary age of Eocene and Oligocene is 33.89 Ma (red words). (b) Depth, Epoch, and age of IODP Hole U1435, SCS (Modified from Li et al., 2016; Shao et al., 2017); the location of Hole U1435 can be found in Fig. 1b; the base age of the Oligocene is 33.9 Ma. (c) Depth, age, Formation, and GR curve of Hole E17, SCS (Modified from Zhang et al., 2020); the boundary age between the Enping and Zhuhai Formation is consistent with the age of the Eocene–Oligocene transition, which is 33.9 Ma. (d) Depth, age, Formation, lithology, and GR curve of Hole K7, SCS (This study); the stratigraphic boundary between the Enping and Zhuhai Formations in Hole K7 is at depths of 2879 m, corresponding to the age of 33.9 Ma. (e) Depth, age, Formation, lithology, and GR curve of Hole S1, SCS (This study); the stratigraphic boundary between the Enping and Zhuhai Formations in Hole S1 is at depths of 2030 m, corresponding to the age of 33.9 Ma. (For interpretation of the references to colour in this figure legend, the reader is referred to the web version of this article.)

(Fig. 3). These samples were mainly composed of SiO_2 and Al_2O_3, with average concentrations of 62.99 wt% and 15.89 wt%, respectively. Moderate concentrations were observed for Fe_2O_3, K_2O, MgO, and Na_2O, with average values of 4.22 wt%, 4.31 wt%, 1.40 wt%, and 1.21 wt%, respectively. The least abundant elements were CaO, TiO_2, P_2O_5, and MnO, with average values of 0.68 wt%, 0.61 wt%, 0.08 wt%, and 0.05 wt%, respectively. The enrichment index (sample/PAAS) for the major elements was calculated based on the average values of the major elements in the post-Archean Australian Shale (PAAS; Mclennan, 1989) (Fig. 3). The samples were generally depleted in Fe_2O_3, MgO, MnO, P_2O_5, and TiO_2, whereas their Al_2O_3, K_2O, SiO_2, and Na_2O contents were comparable to those of PAAS. All data are provided in Supplementary Materials.

4.2. Paleoclimate reconstruction

4.2.1. Paleoweathering

The Enping Formation showed silicate weathering (Fig. 4a), which was characterized by CIA ranging from 63 to 77, with an average of 71; PIA ranging from 75 to 89, with an average of 84; and CIW ranging from 82 to 92, with an average of 88. Conversely, the Zhuhai Formation recorded attenuated silicate weathering, which was characterized by a CIA ranging from 57 to 71, with an average of 62; PIA ranging from 63 to 83, with an average of 72; and CIW ranging from 75 to 87, with an average of 80. Pearson correlation coefficients ($r > 0.99$; $p < 0.01$) demonstrated exceptional covariance among the CIA, PIA, and CIW values, confirming their mutual reliability as quantitative weathering proxies.

4.2.2. Paleoprecipitation and paleotemperature

The reconstructed paleoprecipitation proxies showed similar trends across the profiles (Fig. 4b). For the Enping Formation, MAPa ranged from 1114 to 1342 mm, with an average of 1241 mm; MAPb ranged from 1133 to 1268 mm, with an average of 1211 mm; and MAPc ranged from 807 to 1061 mm, with an average of 963 mm, indicating a humid climate. For the Zhuhai Formation, MAPa ranged from 959 to 1216 mm, with an average of 1068 mm; MAPb ranged from 1025 to 1197 mm, with an average of 1101 mm; and MAPc ranged from 673 to 833 mm, with an average of 732 mm, indicating reduced precipitation.

The results of paleotemperature reconstruction of the Enping Formation show that MATa ranged from 8.5 to 12.7 °C, with an average of 11.2 °C. The range of MATb was 6.4–17.6 °C, with an average of 13.0 °C, indicating that the climate is relatively warm (Fig. 4c). Conversely, the Zhuhai Formation had MATa ranging from 6.9 to 11.1 °C, with an average of 8.6 °C. MATb ranged from 0.93 to 12.5 °C, with an average value of 5.3 °C, indicating that the temperature had decreased (Fig. 4c).

4.3. Paleolake level and paleosalinity

The Mn/(Fe + Ti) × 100 of the Enping Formation ranges from 0.44 to

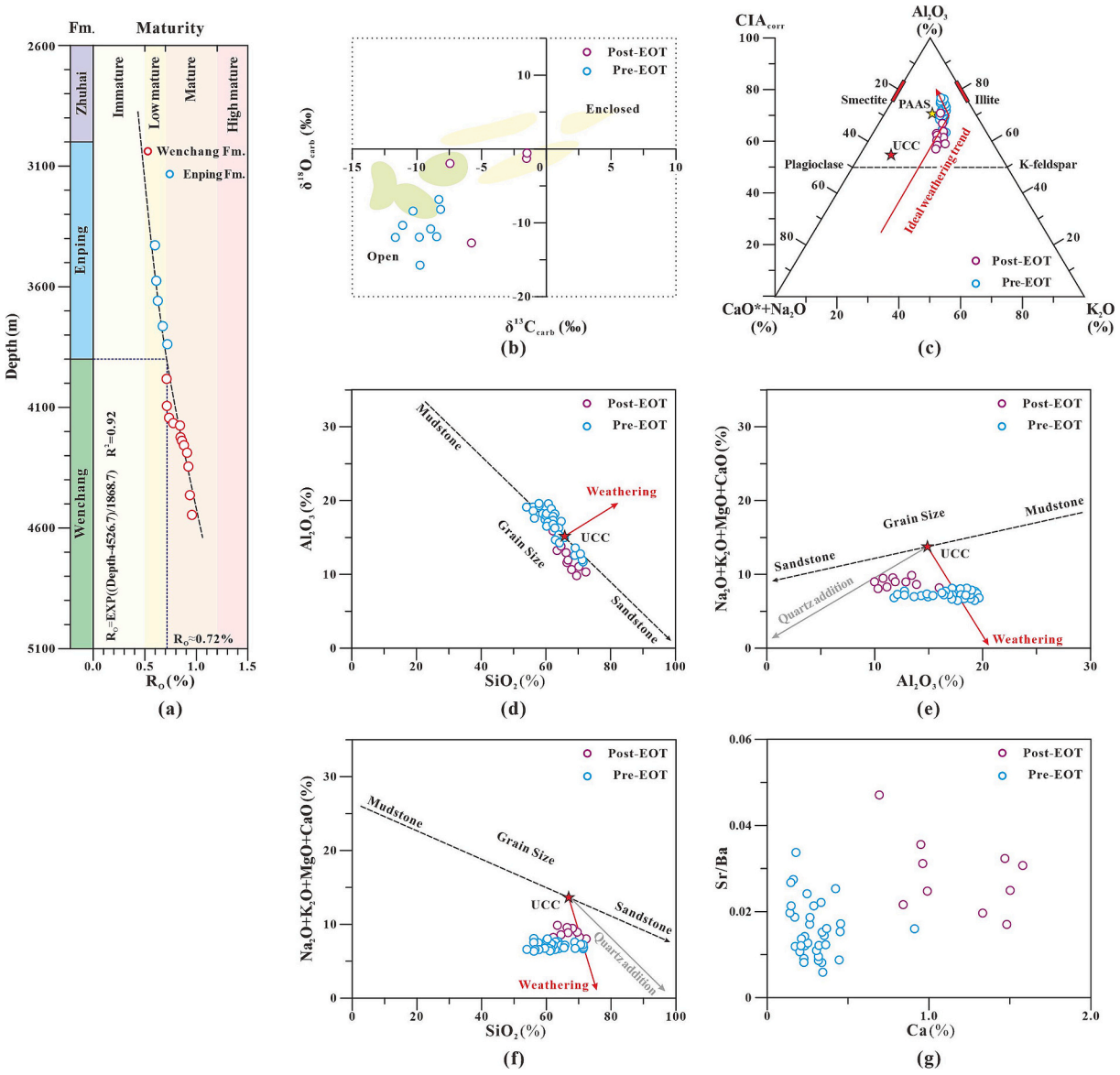

Fig. 6. Eliminating the interference of non-environment factors from environmental proxies. (a) The evolution of sample R_o with depth in Hole K7. (b) The plot of $\delta^{13}C_{carb}$ and $\delta^{18}O_{carb}$ eliminates the interference of non-environment factors (evaporation) from environmental proxies (the template is adapted from Talbot and Kelts, 1990). (c) The diagram of A-CN-K (Al_2O_3-CaO* + Na_2O-K_2O) and the related changes in the corrected CIA for Enping and Zhuhai Formation samples (the template is adapted from Nesbitt and Young, 1982) are used to eliminate the interference of potassium metamorphism on paleoweathering proxies. (d) The plot of Al_2O_3-SiO_2 highlights the grain-size effect, with mud-rich samples containing more aluminum and sand-rich samples containing more silicon. (e) The plot of Na_2O + K_2O + MgO + CaO-SiO_2 eliminates the influence of mineral grain size and quartz enrichment, determining whether the samples are products of primary weathering. (f) The plot of Na_2O + K_2O + MgO + CaO-Al_2O_3 similarly eliminates the influence of mineral grain size and quartz enrichment, determining whether the samples are products of primary weathering. (g) The plot of Sr/Ba-Ca is used to eliminate the influence of calcium enrichment on paleosalinity proxies.

1.79, with an average of 0.95. The Mn/(Fe + Ti) × 100 of the Zhuhai Formation ranges from 0.66 to 3.11, with an average of 1.68. The elemental ratios indicate that the lake level during the Zhuhai Formation period was higher than that of the Enping Formation (Fig. 4d). The GR curve and lithology also reveal the changes in lake level. The high GR curves at the bottom of the Zhuhai Formation in Hole K7 and Hole S1 were interpreted as the deposition of fine-grained rock (Fig. 1c, 5d, e), indicating high lake levels.

Over 78 % of the Enping Formation samples had Sr/Ba ratios that did not exceed 0.02, suggesting that the Enping Formation was deposited in a freshwater environment (Fig. 4e). The Sr/Ba ratios of the Zhuhai Formation ranged from 0.02 to 0.05, with an average of 0.03, indicating a significantly higher paleosalinity than that of the Enping Formation. Additionally, a peak in the Sr/Ba content appeared after 33.9 Ma, marking a shift in paleosalinity (Fig. 4e).

5. Discussion

5.1. Age limitation of the boundary between the enping formation and Zhuhai formation

The T70 interface is an unconformity surface generated by SCS movements and is considered one of the criteria for dividing the Enping and Zhuhai Formations in the PRMB (Fig. 1c). The lithology of the Enping Formation in both Holes K7 and S1 is primarily composed of interbedded sandstones and mudstones, with coal seams, whereas the Zhuhai Formation consists of interbedded sandstones and mudstones with thin limestone (Fig. 5d, e), which is similar to the lithology

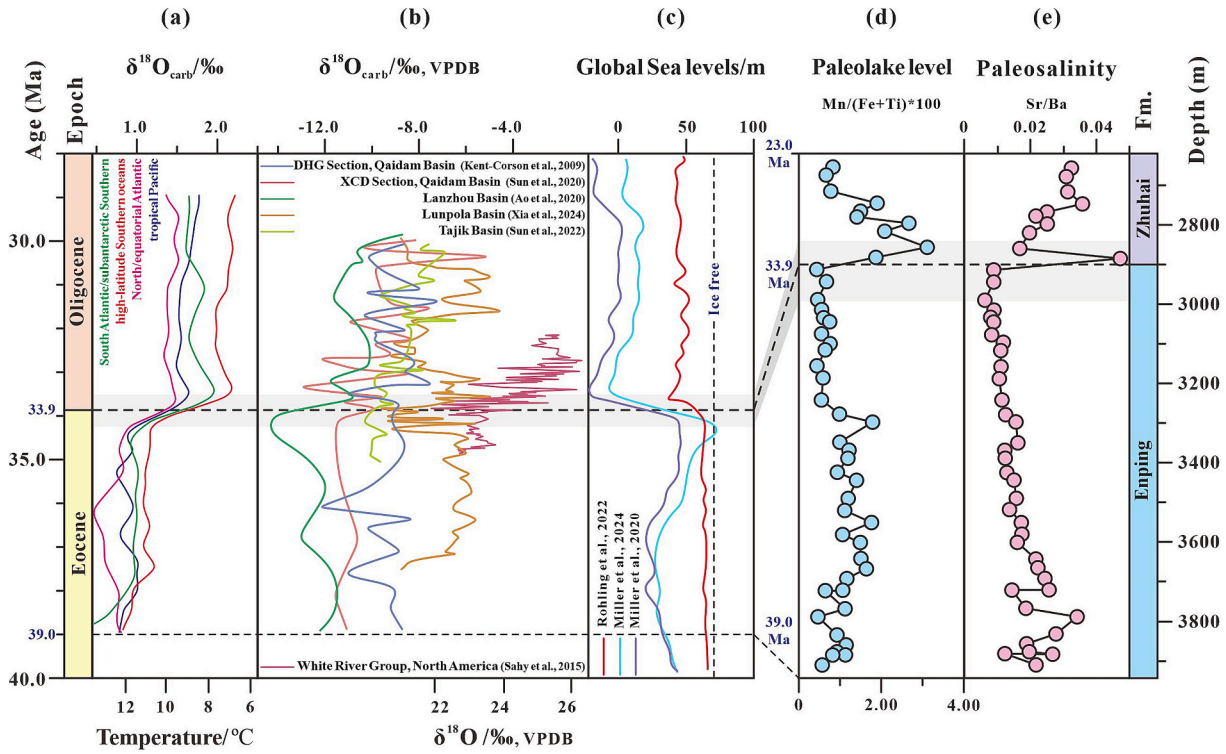

Fig. 7. (a) $\delta^{18}O_{carb}$ from the South Atlantic, high-latitude Southern Ocean, North Equatorial Atlantic, and tropical Pacific (Cramer et al., 2009). (b) $\delta^{18}O_{carb}$ from the Qaidam Basin DHG section (Kent-Corson et al., 2009), XCD section (Sun et al., 2020), Lanzhou Basin (Ao et al., 2020), Lunpola Basin (Xia et al., 2024), and Tajik Basin (Sun et al., 2022), and White River Basin, North America (Sahy et al., 2015). (c) Global sea level changes (Miller et al., 2020; Rohling et al., 2022; Miller et al., 2024). (d) Paleolake level variations in the PRMB. (e) Paleosalinity variations in the PRMB.

combinations observed in the PRMB (Fig. 1c, 5b). Compared with the Zhuhai Formation, the GR log values for the Enping Formation in Holes K7 and S1 were higher and exhibit fluctuations, which was similar to the GR log characteristics recorded in Hole E17 of the PRMB (Fig. 5c; Zhang et al., 2020). Based on the T70 interface, and the sudden changes in the GR and lithology, we determined the stratigraphic boundaries between the Enping and Zhuhai Formations in the Holes K7 and S1 to be at depths of 2879 m and 2030 m, respectively (Fig. 5d, e).

An accurate age model is the foundation for studying deep-time climatic events. The boundary between the Enping and Zhuhai Formations was defined as the boundary between the Eocene and Oligocene as early as 1984 (Qin, 1996). The age of 33.9 Ma is widely accepted, as it is derived from multiple sources, including magnetostratigraphy from Equatorial Pacific sediments (ODP Sites 1218 and 1219), which Lanci et al. (2005) determined to be the EOT age of 33.7 Ma. Previous studies have associated the onset of the opening of the SCS with approximately 33–34 Ma, which corresponds to the boundary age between the Enping and Zhuhai Formations (Li et al., 2014; Wang et al., 2019). Additionally, Li et al. (2016), based the base of the Oligocene in the SCS on the occurrence of *Cassidulinella chipolensis* and T. *ampliapertura* from IODP Hole U1435A, dating it to 33.89 Ma (Fig. 5b). The U—Pb chronology of detrital zircon also showed that the Eocene age of the SCS to be less than 34 Ma, close to the 33.9 Ma measured by planktonic foraminifera (Shao et al., 2017). Zhang et al. (2020) synthesized previous age models, global tectonic and climate evolution, and palynological assemblages from the PRMB, limiting the age of the top boundary of the Enping Formation to 33.9 Ma (Zhang et al., 2020). Given the consistent age across different studies (Wang et al., 2019; Zhang et al., 2020; Peng et al., 2023; Gao et al., 2023, 2024), an age of 33.9 Ma is widely accepted.

The age of 33.9 Ma corresponds to Eocene–Oligocene transition as defined in the GTS2020 (Fig. 5a), validating its use as the boundary age for the Enping and Zhuhai Formations in the PRMB. This age is determined based on multi-proxy evidence, including biostratigraphy, radioisotope dating, magnetostratigraphy, astronomical dating, chemostratigraphy, and climatic evolution (Speijer et al., 2020). The key marker of the EOT is the extinction of the *hantkeninid* planktonic foraminifera at the top of Zone E16, which lies within nannofossil Zone NP21 (Coccioni et al., 1988). K—Ar and Ar—Ar dating of biotite grains from 4.3 m below the base of the EOT give an age of 34.66 ± 0.3 Ma, suggesting a numerical age of about 34 Ma for the EOT itself (Premoli Silva and Jenkins, 1993). The age of EOT was calibrated to 33.9 Ma by using the magnetic stratigraphic age of C13n (33.73 Ma; Fig. 5a) as the basis for constructing astronomical calibration (Westerhold et al., 2014). The EOT event is associated with a positive $\delta^{18}O$ excursion and marked a transition from warm to cold (Zachos et al., 2001), which was synchronized with the cooling of the South China Sea revealed in this study. And the 33.9 Ma as the age of EOT has been widely applied in terrestrial basins, including the Bohai Bay Basin (33.9 Ma; Wu et al., 2025), Beibuwan Basin (33.9 Ma; Liu et al., 2024), Termit Basin (33.9 Ma; Liu et al., 2022), and Jianghan Basin (33.97 Ma; Huang and Hinnov, 2019). Furthermore, Burton et al. (2024) provided evidence for a prominent Eocene–Oligocene unconformity in sedimentary basins along the margins of every continent. The globally widespread Eocene–Oligocene unconformities suggest global controls, of which the extreme climatic and oceanographic changes of the greenhouse to icehouse transition seem particularly compelling.

5.2. *Eliminating the interference of non-environment factors from environmental proxies*

The $\delta^{13}C_{carb}$ and $\delta^{18}O_{carb}$ values reflect dissolved pCO_2 levels in water and temperature (De Boever et al., 2017; Hillaire-Marcel et al., 2021). These isotopic values can be influenced by climate, environment, diagenesis, and thermal evolution (O'Neil et al., 1969; McCormack et al., 2019; Li et al., 2020). Different environments exhibit distinct

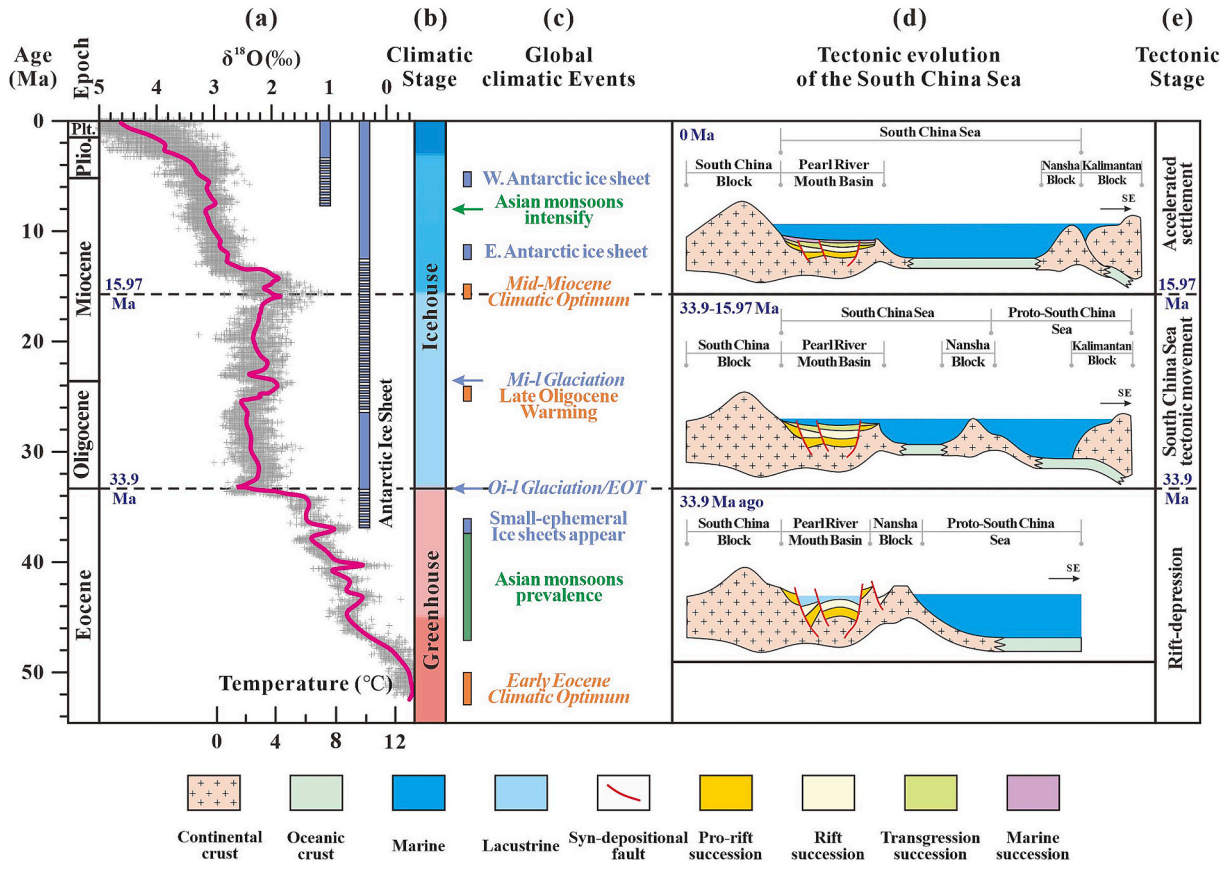

Fig. 8. Coupled evolution of global climate and tectonic evolution of the South China Sea since 54 Ma. (a) Records of global marine $\delta^{18}O$ (modified from Westerhold et al., 2020). (b) Global climate evolution (Pei et al., 2021). (c) Global climatic events (modified from Zachos et al., 2001). (d) Tectonic evolution of the SCS. The SCS originated at ~33.9 Ma through rifting of the Nansha Block from the South China margin, followed by southward subduction. (e) Tectonic evolutionary stages of the PRMB (modified from Holloway, 1982; Taylor and Hayes, 1983; Hinz et al., 1991; Savva et al., 2014; Hall and Breitfeld, 2017; Li et al., 2024a).

carbon and oxygen cycling processes, leading to variations in the isotopic composition of the sediments (Lettéron et al., 2017). In an enclosed water environment (such as inland lakes), evaporation can lead to oxygen isotope enrichment, which affects the $\delta^{18}O$ values in sediments (Talbot and Kelts, 1990). However, during both pre-EOT and post-EOT, the PRMB remained an open system (Fig. 6b), minimizing the impact of evaporation on $\delta^{18}O_{carb}$ values. High thermal evolution conditions can alter isotopic values, potentially masking the original climate signals (Liu et al., 2017). Vitrinite reflectance (R_o) is used to classify the thermal maturity of rock, with the following stages: $R_o < 0.5$ % indicating immature, 0.5 % $< R_o <$ 0.7 % indicating low maturity, 0.7 % $< R_o <$ 1.2 % indicating mature, 1.2 % $< R_o <$ 2.0 % indicating high maturity, and $R_o > 2.0$ % indicating overmature (Bostick and Foster, 1975). In this study, we established an equation for R_o varying with the depth of Hole K7 (Fig. 6a), and predicted that the range of R_o of the Zhuhai and Enping Formations is approximately 0.37–0.72 %, corresponding to the immature-low maturity stage. This suggests that the isotopic values are not significantly affected by diagenesis, and are suitable for paleoclimate reconstruction.

Warm and humid climates intensify the chemical weathering of rocks, thereby altering the elemental geochemical content of sediments (McLennan, 1989; Nesbitt and Young, 1982). Before interpreting weathering proxies as climate proxies, the potential impacts of diagenesis, and grain size variations on sediment elemental composition must be assessed (Li et al., 2020; Tang et al., 2024). The discussions of the thermal evolution above have confirmed that the Enping and Zhuhai Formations are nearly unaffected by diagenesis (Fig. 6a).

Sedimentary recycling refers to the weathering, erosion, transportation, and deposition of sediments after initial deposition or diagenesis. The diagram of Al_2O_3-(CaO* + Na_2O)-K_2O (A-CN-K) reflects the initial weathering rate of sediments (Fedo et al., 1995; Nesbitt and Young, 1982) and determines whether sediments have undergone multiple weathering and deposition (Garzanti et al., 2013; Garzanti and Resentini, 2016). In the A-CN-K ternary diagram, the samples are distributed parallel to the A-CN or A-K axis (Fig. 6c), suggesting that most sediments follow the ideal trend line of chemical weathering with no potassium enrichment (Garzanti et al., 2013; Tang et al., 2024). The Al_2O_3-SiO_2 plot highlights the grain-size effect, with the samples of the Eocene Enping Formation and Oligocene Zhuhai Formation following the grain size trend (Fig. 6d). Furthermore, the $Na_2O + K_2O + MgO +$ CaO-Si_2O and $Na_2O + K_2O + MgO +$ CaO-Al_2O_3 plots show that the data are parallel to the empirical lines of grain size and close to the weathering line (Fig. 6e, f). These results suggest that the chemical weathering proxies in the PRMB reflect primary weathering associated with changes in the original paleoenvironment. Thus, it is convincing to quantitatively reconstruct the paleoclimate by using the major elements of the Eocene Enping Formation and Oligocene Zhuhai Formation in the PRMB.

The Sr in lake sediments has two main sources: detrital parent rock fragments and carbonate compounds (Zeng et al., 2011). Therefore, before using Sr/Ba as a proxy to evaluate paleosalinity, the influence of carbonate minerals (Ca content) on the Sr content must be excluded (Wei and Algeo, 2020; Li et al., 2020). The Sr/Ba content of the samples from the SCS did not show enrichment with increasing Ca content (Fig. 6g), indicating that the Sr/Ba ratio is not influenced by carbonate rocks and can be reliably used for paleosalinity reconstruction.

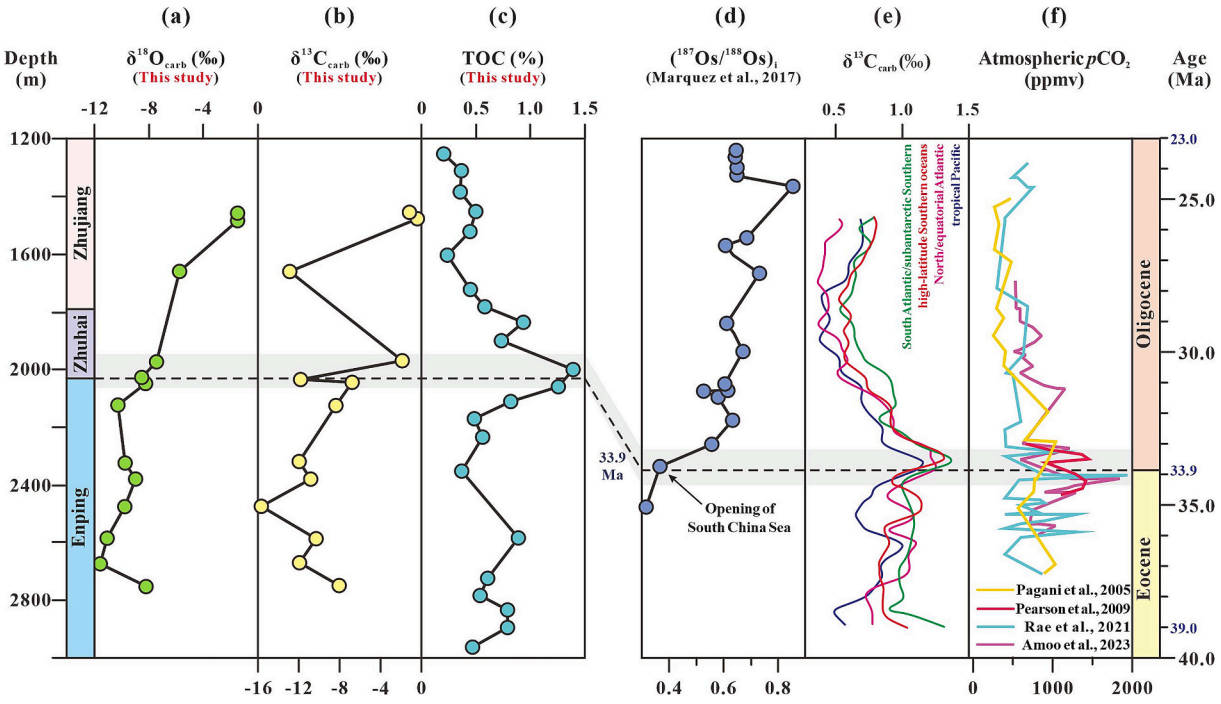

Fig. 9. Multi-proxy paleoenvironmental records from the SCS (SCS) during the Late Eocene–Early Oligocene transition and global marine isotope and atmospheric CO_2 levels. (a) $\delta^{18}O_{carb}$ records from PRMB. (b) $\delta^{18}O_{carb}$ records from PRMB. (c) TOC contents of PRMB. (d) Osmium isotope ($^{187}Os/^{186}Os$) records from SCS sediments (Marquez et al., 2017). (e) Comparative $\delta^{13}C$ records from South Atlantic, high-latitude Southern Ocean, North Equatorial Atlantic, and tropical Pacific (Cramer et al., 2009). (f) Compilation of atmospheric CO_2 reconstructions using multiple proxies (Pagani et al., 2005; Pearson et al., 2009; Rae et al., 2021; Amoo et al., 2023).

5.3. EOT records of the SCS

5.3.1. The global significance of the EOT record in the SCS

Our paleoclimatic reconstruction of the SCS, spanning the Late Eocene to Early Oligocene, revealed critical environmental transitions. At 33.9 Ma, the SCS experienced a marked shift from intense to moderate chemical weathering, as evidenced by 15, 21, and 13 reductions in CIA, PIA, and CIW values, respectively (Fig. 4a). These trends are corroborated by CIA_{corr} records (Fig. 6c) and are consistent with diminished chemical weathering signals from coeval terrestrial basins (Lühe Basin and Tajik Basin, Tibetan Plateau), as documented through major element ratios (Sun et al., 2022; Tang et al., 2024).

The coal-bearing strata of the Enping Formation attest to sustained high precipitation during the Late Eocene (Stach et al., 1982; Korasidis et al., 2019), which is consistent with our reconstructed high MAP. However, MAPa, MAPb, and MAPc declines of 283 mm, 187 mm, and 281 mm occurred at 33.9 Ma (Fig. 4b), synchronizing with the aridification in southeastern Australia from palynological evidence (Sluiter et al., 2022) and precipitation reduction in North America from geochemical indicators (Sheldon et al., 2002). This synchronicity demonstrates a global continental climate transition from humid to arid conditions during the EOT.

Significant cooling was also recorded in the terrestrial sediments of the SCS, as evidenced by a decrease of 4.4 °C and 9.4 °C in MATa and MATb (Fig. 4c), respectively, and an approximately 1.0 ‰ positive $\delta^{18}O_{carb}$ excursion (Fig. 9a). This paleotemperature trend is consistent with the climate changes recorded by major element proxies and palynological assemblages in the marine sediments of the SCS (Wu et al., 2003). Furthermore, the cooling of the SCS is synchronous with records from global marine and terrestrial basins (Zachos et al., 2001; Cramer et al., 2009; Kent-Corson et al., 2009; Li et al., 2016; Sun et al., 2020; Sluiter et al., 2022; Sun et al., 2022; Akabane et al., 2024; Tang et al., 2024; Xia et al., 2024), suggesting that the climate transition during the EOT was global in nature (Sahy et al., 2015).

5.3.2. The uniqueness of the EOT records in the SCS

The EOT paleoclimate record from the SCS shows temporal consistency with the global marine and terrestrial records (Fig. 7a, 7b). However, lake level changes exhibit spatial heterogeneity. The GR logging curves in Holes K7 and S1 show a significant increase at the bottom of the Zhuhai Formation, which is interpreted as the deposition of mudstone, indicating weak hydrodynamic conditions and high lake levels. Elemental geochemical proxies also confirm that around 33.9 Ma, the PRMB experienced its highest lake level since the Cenozoic (Fig. 7d), which contrasts with the significant global sea level decline during the EOT (Fig. 7c). Following this maximum, lake levels in the SCS responded in line with global sea level changes (Fig. 7d).

5.4. Opening of SCS forcing the cooling at EOT

The EOT event was initially characterized by cooling in the Southern Hemisphere and the formation of the Antarctic ice sheet (Coxall et al., 2005; Liu et al., 2009; Pagani et al., 2011). The opening of the Tasman Gateway and Drake Passage is considered to have accelerated the development of the Antarctic Circumpolar Current, contributing to global climate cooling and ice sheet growth (Kennett et al., 1974; Kennett, 1977; Zachos et al., 2001; Lagabrielle et al., 2009; Cristini et al., 2012; Scher et al., 2015). During this period, analogous tectonic reorganizations involving marine gateway development occurred globally, including in the SCS (e.g., Gruetzner et al., 2022; Piller et al., 2024). Prior to the EOT, the PRMB was in a rifting evolutionary stage (Briais et al., 1993). At 33.9 Ma, the lithospheric breakup of the South China Block (Fig. 8d) initiated the opening of the SCS (Barckhausen et al., 2014; Wu et al., 2016; Wu and Suppe, 2018). Multiple lines of evidence, including paleomagnetic records (Li et al., 2014, 2016), seawater osmium isotope records (Marquez et al., 2017), petrological analyses (Wang et al., 2023b; Fournier et al., 2024), and palynological data (Cheng et al., 2023), collectively corroborate the timing of this marine opening event. Following its detachment from the South China Block,

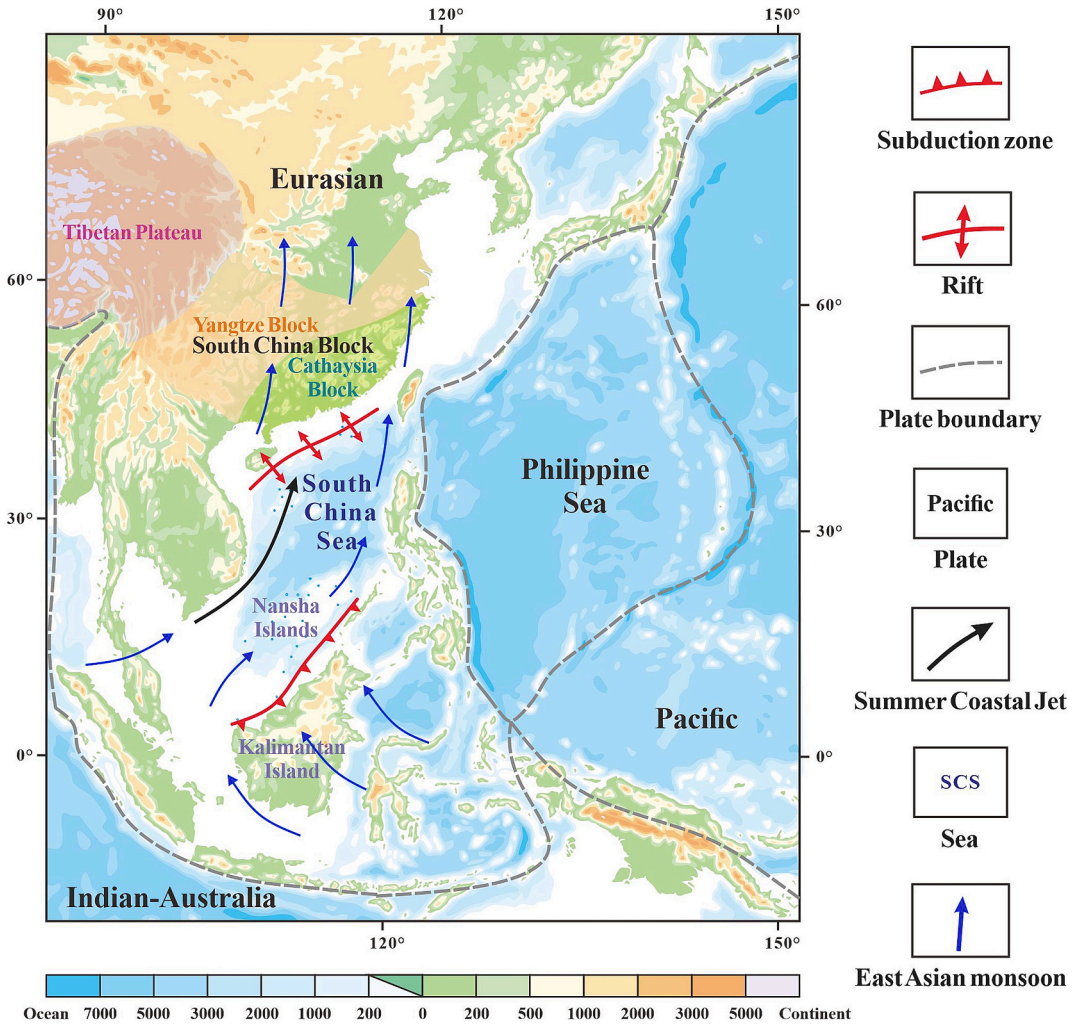

Fig. 10. Modern monsoon and oceanic current patterns in Southeast Asia. Blue arrows indicate prevailing East Asian Monsoon directions (modified from Fournier et al., 2024). Black arrows denote summer coastal currents in the SCS (modified from Li et al., 2023; Fournier et al., 2024). (For interpretation of the references to colour in this figure legend, the reader is referred to the web version of this article.)

the Nansha Block migrated southward and was ultimately subducted beneath Kalimantan Island at 15.97 Ma (Holloway, 1982; Taylor and Hayes, 1983; Hall and Breitfeld, 2017; Li et al., 2024a), establishing the present geomorphological configuration (Fig. 10). Notably, this tectonic interval (33.9–15.97 Ma) corresponds temporally with the Oligocene–Middle Miocene glaciation stage (Fig. 8). This temporal correlation suggests a potential link between the tectonic evolution of the PRMB and regional climatic cooling through tectonic forcing mechanisms.

Marquez et al., 2017 identified osmium isotope anomalies in SCS sediments, providing evidence of increased oceanic connectivity between the SCS and global circulation during the EOT (Fig. 9d). This enhanced connectivity likely played an important role in facilitating the influx of cool water masses into the SCS (Fournier et al., 2024). The resulting thermohaline forcing amplified coastal upwelling, which was preserved in the Early Oligocene biogenic-rich carbonate strata within the SCS, coinciding with the opening of the SCS (Fournier et al., 2024). This upwelling was similar to the modern oceanic circulation in Southeast Asia (Fig. 10). This upwelling led to an increase in nutrient fluxes, promoting a productivity bloom, as evidenced by biogenic-rich strata in the NW Palawan Block and elevated TOC content in the Hole records at 33.9 Ma (Fig. 9c; Diester-Haass and Zahn, 2001, 1996; Fournier et al., 2024). A parallel mechanism was observed in the Atlantic, where the closure of the Tethyan Seaways triggered the influx of cool deep waters, driving benthic foraminiferal turnover (Coccioni and Galeotti, 2003; Allen and Armstrong, 2008). Globally, marine carbonate $\delta^{13}C$ (Fig. 9e) and terrestrial $\delta^{13}C$ (Korasidis et al., 2019; Chaanda et al., 2023; Rull, 2023) positive excursions further support the idea of enhanced organic carbon sequestration by marine and terrestrial systems during the EOT (Fig. 9b; Sun et al., 2014). This organic carbon burial effectively sequesters CO_2 from the atmosphere, thereby reducing the greenhouse effect and supporting the cooling trend (Anderson and Delaney, 2005). As atmospheric pCO_2 levels decreased, this feedback loop further amplified global climate cooling, as evidenced by geochemical data (Fig. 9f). Therefore, the cooling during the EOT in the SCS resulted from a dual mechanism: (1) tectonically driven oceanic reorganization that altered heat transport, and (2) a decline in pCO_2 levels linked to enhanced organic productivity and subsequent carbon sequestration.

5.5. *Opening of SCS forcing the lake level rise at EOT*

The global sea level decline during the EOT has been attributed to global climatic cooling and the onset of Antarctic glaciation (Miller et al., 2020). Our study reveals a notable anomaly in the SCS during this interval, where an initial lake-level rise of the PRMB preceded a subsequent decline, contrasting with global trends. This divergence from global eustatic patterns necessitates a re-examination of the underlying mechanisms. The sudden increase in paleosalinity provides evidence for

the rise in lake levels in the PRMB. Liang et al. (2024) identified four salinization mechanisms: evaporative concentration under aridity, deep hydrothermal influx, marine transgression, and their combinations. The paleo-SCS, situated below approximately 23°N (Zhang et al., 2018), maintained humid conditions with a MAP exceeding 600 mm despite EOT aridification (Fig. 4b). This precludes evaporative salinization under moisture-deficit conditions (Eugster and Hardie, 1978; Gasse et al., 2008; Chen, 2020). During the EOT, lake sediments in the PRMB did not record evidence of hydrothermal fluids, effectively eliminating hydrothermal contributions to increased paleosalinity (Fig. 7e).

Tectonic movements play a key role in sea transgression and regression events, as they determine the beginning and end of such events by opening and closing gateways for seawater movement at the basin edge (Schulz et al., 2005; Sun et al., 2016). The sudden increase in paleosalinity at 33.9 Ma is consistent with lithospheric fractures caused by SCS movement and explains the sudden increase in lake levels (Fig. 4d). This tectonic reorganization facilitated marine transgression, as evidenced by marine planktonic foraminiferal blooms in the Zhuhai Formation strata (Li et al., 2016; Zhang et al., 2020) and a progressive facies transition from continental to marine environments with thin marine limestone deposition (Li et al., 2017; Fig. 1c, 5c, d). The observed spatial heterogeneity in the PRMB paleolake level relative to global sea-level trends reflects tectonic forcing. Post-tectonic stabilization trends of lake levels presented global synchronicity. Therefore, the opening of the SCS served two roles: 1) as a tectonic driver amplifying EOT cooling through altered ocean-atmosphere circulation, and 2) as the primary control on hydrological decoupling between the SCS and global records during this climate transition.

6. Conclusions

1. The PRMB preserves crucial terrestrial records of environmental changes during the EOT. At 33.9 Ma, the SCS experienced rapid reductions in weathering, temperature, and precipitation, along with a lake level rise. While paleoclimatic changes are consistent with global cooling trends, its lake levels exhibit spatial heterogeneity from contemporaneous global sea-level decline.
2. We established a novel causal link between the opening of the SCS and cooling at 33.9 Ma. This tectonic event facilitated the reorganization of ocean circulation, promoting upwelling and reducing atmospheric CO_2 through increased biological productivity and ultimately driving climatic cooling.
3. The opening of the SCS serves as a distinct tectonic mechanism for regional hydrological changes during the EOT, which differs from global patterns. The rise in lake levels was driven by transgression, a consequence of tectonic reorganization.

CRediT authorship contribution statement

Jing Guo: Writing – original draft, Visualization, Software, Conceptualization. **Fujie Jiang:** Writing – review & editing, Project administration, Funding acquisition. **Guangrong Peng:** Resources, Funding acquisition. **Yuqi Wu:** Writing – review & editing, Software, Methodology. **Weibing Shen:** Writing – review & editing, Supervision. **Rui Zhang:** Validation, Investigation. **Yu An:** Supervision. **Dapeng Jiang:** Formal analysis, Conceptualization. **Fusheng Yu:** Software, Formal analysis. **Yaqi Li:** Visualization. **Zhifeng Yu:** Methodology. **Jiabing Jiang:** Software.

Declaration of competing interest

None.

Appendix A. Supplementary data

Supplementary data to this article can be found online at https://doi.org/10.1016/j.palaeo.2025.113164.

Data availability

The authors confirm that all data necessary for supporting the scientific findings of this paper have been provided.

References

Akabane, T.K., Garcia, M.J., Kern, A.K., De Oliveira, P.E., 2024. Eocene–Oligocene vegetation and climate changes in southeastern Brazil. Rev. Palaeobot. Palynol. 327, 105142. https://doi.org/10.1016/j.revpalbo.2024.105142.

Allen, M.B., Armstrong, H.A., 2008. Arabia–Eurasia collision and the forcing of mid-Cenozoic global cooling. Palaeogeogr. Palaeoclimatol. Palaeoecol. 265, 52–58. https://doi.org/10.1016/j.palaeo.2008.04.021.

Amoo, M., Salzmann, U., Pound, M.J., Hoem, F.S., Thompson, N., Bijl, P.K., 2023. Late Eocene to late Oligocene terrestrial climate and vegetation change in the western Tasmanian region. Palaeogeogr. Palaeoclimatol. Palaeoecol. 623, 111632. https://doi.org/10.1016/j.palaeo.2023.111632.

Anderson, L.D., Delaney, M.L., 2005. Middle eocene to early Oligocene paleoceanography from Agulhas Ridge, Southern Ocean (Ocean Drilling Program Leg 177, Site 1090). Paleoceanography 20, PA1013. https://doi.org/10.1029/2004PA001043.

Ao, H., Dupont-Nivet, G., Rohling, E.J., Zhang, P., Ladant, J.-B., Roberts, A.P., Licht, A., Liu, Q., Liu, Z., Dekkers, M.J., Coxall, H.K., Jin, Z., Huang, C., Xiao, G., Poulsen, C.J., Barbolini, N., Meijer, N., Sun, Q., Qiang, X., Yao, J., An, Z., 2020. Orbital climate variability on the northeastern Tibetan Plateau across the Eocene–Oligocene transition. Nat. Commun. 11, 5249. https://doi.org/10.1038/s41467-020-18824-8.

Barckhausen, U., Engels, M., Franke, D., Ladage, S., Pubellier, M., 2014. Evolution of the South China Sea: revised ages for breakup and seafloor spreading. Mar. Pet. Geol. 58, 599–611. https://doi.org/10.1016/j.marpetgeo.2014.02.022.

Bosboom, R., Dupont-Nivet, G., Grothe, A., Brinkhuis, H., Villa, G., Mandic, O., Stoica, M., Huang, W., Yang, W., Guo, Z., Krijgsman, W., 2014. Linking Tarim Basin sea retreat (West China) and Asian aridification in the late Eocene. Basin Res. 26, 621–640.

Bostick, N.H., Foster, J.N., 1975. Comparison of vitrinite reflectance in coal seams and in kerogen of sandstones, shales, and limestones in the same part of a sedimentary section. In: Alpern (Ed.), Pétrographie de la Matière. Organique des Sédiments, CNRS, Paris, pp. 13–25.

Briais, A., Patriat, P., Tapponnier, P., 1993. Updated interpretation of magnetic anomalies and seafloor spreading stages in the South China Sea: Implications for the Tertiary tectonics of Southeast Asia. J. Geophys. Res. 98, 6299–6328. https://doi.org/10.1029/92JB02280.

Chaanda, M.S., Grimes, S.T., Jerrett, R.M., Anderson, M., Leng, M.J., Fitzpatrick, M.E., Price, G.D., 2023. Terrestrial carbon isotope stratigraphy of the Eocene–Oligocene transition, Petrockstowe and Bovey basins, Devon, UK. Proc. Geol. Assoc. 134, 517–525. https://doi.org/10.1016/j.pgeola.2023.05.003.

Chen, W.K., 2020. Sedimentary System Characteristics of Rift Strata in the Great Campos Basin. Eastern Brazil.

Cheng, Z., Ma, R., Cao, L., Liu, C., Dai, L., Weng, C., 2023. Rapid reorganization of the Pearl River network driven by spreading of the South China Sea at around 32 Ma. Palaeogeogr. Palaeoclimatol. Palaeoecol. 629, 111786. https://doi.org/10.1016/j.palaeo.2023.111785.

Coccioni, R., Galeotti, S., 2003. Deep-water benthic foraminiferal events from the Massignano Eocene/Oligocene boundary stratotype, Central Italy. In: Prothero, D.R., Ivany, L.C., Nesbitt, E.A. (Eds.), From Greenhouse to Icehouse: The Marine Eocene–Oligocene Transition. Columbia University Press, New York, pp. 438–453.

Coccioni, R., Monaco, P., Monechi, S., Nocchi, M., Parisi, G., 1988. Biostratigraphy of the Eocene–Oligocene boundary at Massignano (Ancona, Italy). In: Premoli Silva, I., Coccioni, R., Montanari, A. (Eds.), The Eocene-Oligocene Boundary in the Marche-Umbria Basin (Italy). International Subcommission on Paleogene Stratigraphy, Ancona, pp. 59–80.

Colwyn, D.A., Hren, M.T., 2019. An abrupt decrease in Southern Hemisphere terrestrial temperature during the Eocene–Oligocene transition. Earth Planet. Sci. Lett. 512, 227–235.

Coxall, H.K., Wilson, P.A., Pälike, H., Lear, C.H., Backman, J., 2005. Rapid stepwise onset of Antarctic glaciation and deeper calcite compensation in the Pacific Ocean. Nature 433, 53–57.

Coxall, H.K., Wilson, P.A., Pälike, H., 2011. Early Oligocene glaciation and productivity in the eastern equatorial Pacific: insights into global carbon cycling. Paleoceanography 26, PA2221. https://doi.org/10.1029/2010PA002021.

Cramer, B.S., Toggweiler, J.R., Wright, J.D., Katz, M.E., Miller, K.G., 2009. Ocean overturning since the late cretaceous: Inferences from a new benthic foraminiferal isotope compilation. Paleoceanography 24, PA4216.

Cristini, L., Grosfeld, K., Butzin, M., Lohmann, G., 2012. Influence of the opening of the Drake Passage on the Cenozoic Antarctic Ice Sheet: a modeling approach. Palaeogeogr. Palaeoclimatol. Palaeoecol. 339–341, 66–73.

De Boever, E., Brasier, A.T., Foubert, A., Kele, S., 2017. What do we really know about early diagenesis of non-marine carbonates? Sediment. Geol. 361, 25–51. https://doi.org/10.1016/j.sedgeo.2017.09.011.

DeConto, R.M., Pollard, D., 2003. Rapid Cenozoic glaciation of Antarctica induced by declining atmospheric CO_2. Nature 421, 245–249.

Diester-Haass, L., Zahn, R., 1996. Eocene–Oligocene transition in the Southern Ocean: history of water mass circulation and biological productivity. Geology 24, 163–166.
Diester-Haass, L., Zahn, R., 2001. Paleoproductivity increase at the Eocene–Oligocene climatic transition: ODP/DSDP sites 763 and 592. Palaeogeogr. Palaeoclimatol. Palaeoecol. 172, 153–170.
Egan, K.E., Rickaby, R.E.M., Hendry, K.R., Halliday, A.N., 2013. Opening the gateways for diatoms primes Earth for Antarctic glaciations. Earth Planet. Sci. Lett. 375, 34–43.
Eugster, H.P., Hardie, L.A., 1978. Saline Lakes. In: Lerman, A. (Ed.), Lakes: Chemistry, Geology, Physics. Springer, New York, New York, NY, pp. 237–293.
Farhaduzzaman, M., Abdullah, W., Islam, M., 2012. Depositional environment and hydrocarbon source potential of the Permian Gondwana coals from the Barapukuria Basin, Northwest Bangladesh. Int. J. Coal Geol. 90, 162–179. https://doi.org/10.1016/j.coal.2011.12.006.
Fedo, C.M., Nesbitt, H.W., Young, G.M., 1995. Unraveling the effects of potassium metasomatism in sedimentary rocks and paleosols, with implications for paleoweathering conditions and provenance. Geology 23, 921–924.
Fournier, F., Teillet, T., Licht, A., Borgomano, J., Montaggioni, L., 2024. Eocene–Oligocene large-scale circulation of the East Asian summer monsoon recorded in neritic carbonates of the proto-South China Sea. Palaeogeogr. Palaeoclimatol. Palaeoecol. 633, 111883. https://doi.org/10.1016/j.palaeo.2023.111883.
Gao, Y., Peng, G., Chen, Z., et al., 2023. Breakthrough and significance of deep-water paleogene exploration in Kaiping sag, Pearl River Mouth Basin. Acta Pet. Sin. 44 (7), 1029–1040. https://doi.org/10.7623/syxb202307001.
Gao, Y., Long, Z., Chen, C., et al., 2024. Geochemical characteristics and genesis of middle and deep oil in Southern Region of Kaiping Sag, Pearl River Mouth Basin. J. Jilin University Earth Sci. Edit. 54 (6), 1883–1895. https://doi.org/10.13278/j.cnki.jjuese.20240248.
Garzanti, E., Resentini, A., 2016. Provenance control on chemical indices of weathering (Taiwan river sands). Sediment. Geol. 336, 81–95. https://doi.org/10.1016/j.sedgeo.2015.06.013.
Garzanti, E., Padoan, M., Setti, M., Najman, Y., Peruta, L., Villa, I.M., 2013. Weathering geochemistry and Sr-Nd fingerprints of equatorial upper Nile and Congo muds. Geochem. Geophys. Geosyst. 14, 292–316.
Gasse, F., Chalie, F., Vincens, A., Williams, M.A.J., Williamson, D., 2008. Climatic patterns in equatorial and southern Africa from 30,000 to 10,000 years ago reconstructed from terrestrial and near-shore proxy data. Quat. Sci. Rev. 27, 2316–2340. https://doi.org/10.1016/j.quascirev.2008.06.017.
Gruetzner, J., Matthiessen, J., Geissler, W.H., Gebhardt, A.C., Schreck, M., 2022. A revised core-seismic integration in the Molloy Basin (ODP Site 909): implications for the history of ice rafting and ocean circulation in the Atlantic-Arctic gateway. Glob. Planet. Chang. 215, 103876. https://doi.org/10.1016/j.gloplacha.2022.103876.
Hall, R., Breitfeld, H.T., 2017. Nature and demise of the Proto-South China Sea. Bull. Geol. Soc. Malaysia 63, 61–76. https://doi.org/10.7186/bgsm63201703.
Harnois, L., 1988. The CIW index: a new chemical index of weathering. Sediment. Geol. 55 (3–4), 319–322. https://doi.org/10.1016/0037-0738(88)90137-6.
Herman, F., Seward, D., Valla, P., Carter, A., Kohn, B., Willett, S.D., Ehlers, T.A., 2013. Worldwide acceleration of mountain erosion under a cooling climate. Nature 504, 423–426. https://doi.org/10.1038/nature12877.
Hillaire-Marcel, C., Kim, S.T., Landais, A., Ghosh, P., Assonov, S., Lécuyer, C., Blanchard, M., Meijer, H.A.J., Steen-Larsen, H.C., 2021. A stable isotope toolbox for water and inorganic carbon cycle studies. Nat. Rev. Earth Environ. 2 (10), 699–719. https://doi.org/10.1038/s43004-021-0699-2.
Hinz, K., Block, M., Kudrass, H.R., Meyer, H., 1991. Structural elements of the Sulu Sea, Philippines. Geologisches Jahrbuch: Reihe A 127, 483–506.
Holloway, N.H., 1982. North Palawan Block, Philippines—its relation to Asian mainland and role in evolution of South China Sea. AAPG Bull. 66, 1355–1383. https://doi.org/10.1306/03B5A7A5-16D1-11D7-8645000102C1865D.
Houben, A.J., Bijl, P.K., Pross, J., Bohaty, S.M., Passchier, S., Stickley, C.E., Rohl, U., Sugisaki, S., Tauxe, L., van de Flierdt, T., Olney, M., Sangiorgi, F., Sluijs, A., Escutia, C., Brinkhuis, H., the Expedition 318 Scientists, 2013. Reorganization of Southern Ocean plankton ecosystem at the onset of Antarctic glaciation. Science 340 (6130), 341–344. https://doi.org/10.1126/science.1233980.
Huang, C., Hinnov, L., 2019. Astronomically forced climate evolution in a saline lake record of the middle Eocene to Oligocene, Jianghan Basin, China. Earth Planet. Sci. Lett. 529, 115846. https://doi.org/10.1016/j.epsl.2019.115846.
Jicha, B.R., Scholl, D.W., Rea, D.K., 2009. Circum-Pacific arc flare-ups and global cooling near the Eocene Oligocene boundary. Geology 37 (4), 303–306. https://doi.org/10.1130/gsa.2009.1.1051.
Katz, M.E., Miller, K.G., Wright, J.D., Wade, B.S., Browning, J.V., Cramer, B.S., Rosenthal, Y., 2008. Stepwise transition from the Eocene greenhouse to the Oligocene icehouse. Nat. Geosci. 1, 329–334. https://doi.org/10.1038/ngeo244.
Kennett, J.P., 1977. Cenozoic evolution of Antarctic glaciation, the circum-Antarctic Ocean, and their impact on global paleoceanography. J. Geophys. Res. 82, 3843–3860. https://doi.org/10.1029/JGR082i027p03843.
Kennett, J.P., Houtz, R.E., Andrews, P.B., Edwards, A.R., Gostin, V.A., Hajos, M., Hampton, M.A., Jenkins, D.G., Margolis, S.V., Ovenshine, A.T., Perch-Nielsen, K., 1974. Development of the Circum-Antarctic current. Science 186, 144–147. https://doi.org/10.1126/science.186.4158.144.
Kent-Corson, M.L., Ritts, B.D., Zhuang, G., Bovet, P.M., Graham, S.A., Page Chamberlain, C., 2009. Stable isotopic constraints on the tectonic, topographic, and climatic evolution of the northern margin of the Tibetan Plateau. Earth Planet. Sci. Lett. 282, 158–166. https://doi.org/10.1016/j.epsl.2009.03.019.
Korasidis, V.A., Wallace, M.W., Wagstaff, B.E., Hill, R.S., 2019. Terrestrial cooling record through the Eocene–Oligocene transition of Australia. Glob. Planet. Chang. 173, 61–72. https://doi.org/10.1016/j.gloplacha.2018.12.007.
Lagabrielle, Y., Goddéris, Y., Donnadieu, Y., Malavieille, J., Suarez, M., 2009. The tectonic history of Drake Passage and its possible impacts on global climate. Earth Planet. Sci. Lett. 279, 197–211. https://doi.org/10.1016/j.epsl.2009.01.022.
Lanci, L., Parés, J.M., Channell, J.E.T., Kent, D.V., 2005. Oligocene magnetostratigraphy from Equatorial Pacific sediments (ODP Sites 1218 and 1219, Leg 199). Earth Planet. Sci. Lett. 237 (3–4), 617–634. https://doi.org/10.1016/j.epsl.2005.07.004.
Lear, C.H., Bailey, T.R., Pearson, P.N., Coxall, H.K., Rosenthal, Y., 2008. Cooling and ice growth across the Eocene–Oligocene transition. Geology 36, 251–254. https://doi.org/10.1130/gsa.2008.1.0251.
Lettéron, A., Luterbacher, H., Foerster, A., 2017. Multi-proxy paleoenvironmental reconstruction of saline lake carbonates: paleoclimatic and paleogeographic implications (Priabonian-Rupelian, Issirac Basin, SE France). Sediment. Geol. 358, 42–57. https://doi.org/10.1016/j.sedgeo.2017.04.005.
Li, P., 1993. Cenozoic tectonic movement in the Pearl River Mouth Basin. China Offshore Oil Gas 7 (6), 11–17.
Li, C., Xu, X., Lin, J., et al., 2014. Ages and magnetic structures of the South China Sea constrained by deep tow magnetic surveys and IODP Expedition 349. Geochem. Geophys. Geosyst. 15, 4958–4983. https://doi.org/10.1002/2014GC005553.
Li, Q., Cheng, X., Chen, J., et al., 2016. Data report: oligocene foraminifers and stable isotopes from IODP Hole U1435A. Proc. Int. Ocean Discov. Prog. 349, 1–5. https://doi.org/10.1437/iodp.proc.349.2016.
Li, Q., Wu, G., Zhang, L., et al., 2017. Paleogene marine deposition records of rifting and breakup of the South China Sea: an overview. Sci. China Earth Sci. 60, 2128–2140. https://doi.org/10.1007/s11430-017-9111-8.
Li, Y., Sun, P., Liu, Z., Wang, J., Li, Y., Zhang, M., 2020. Geochemistry of the Permian oil shale in the Northern Bogda mountain, Junggar Basin, Northwest China: implications for weathering, provenance, and tectonic setting. ACS Earth Sp Chem. https://doi.org/10.1021/acsearthspacechem.0c00113.
Li, F., Yang, S., Breecker, D.O., Ramos, E.J., Huang, X., Duan, Z., Guo, Y., Li, C., Mei, X., 2022. Responses of silicate weathering intensity to the Pliocene-Quaternary cooling in East and Southeast Asia. Earth Planet. Sci. Lett. 578. https://doi.org/10.1016/j.epsl.2022.117324.
Li, M., Wan, S., Colin, C., Jin, H., Zhao, D., Pei, W., Jiao, W., Tang, Y., Tan, Y., Shi, X., Li, A., 2023. Expansion of C4 plants in South China and evolution of East Asian monsoon since 35 Ma: Black carbon records in the northern South China Sea. Glob. Planet. Chang. 223, 104079. https://doi.org/10.1016/j.gloplacha.2023.104079.
Li, Y., Gong, C., Qiu, X., Breitfeld, H.T., Barbarand, J., Colin, C., 2024a. Provenance history of the eastern Pearl River Mouth Basin: Implications for the evolution of the South China margin. Mar. Pet. Geol. 136 (11–12), 5191–5207. https://doi.org/10.1130/B37568.1.
Li, Y., Sun, P., Zhang, Q., Wang, J., 2024b. Quantitative geochemical reconstruction of Eocene paleoenvironment in Fushun Basin, Northeast China. Acta Geochim. 43 (3), 571–587.
Liang, C., Yang, B., Cao, Y., Liu, K., Wu, J., Hao, F., Han, Y., Han, W., 2024. Salinization mechanism of lakes and controls on organic matter enrichment: from present to deep-time records. Earth Sci. Rev. 251, 104720. https://doi.org/10.1016/j.earscirev.2024.104720.
Liu, Z., Pagani, M., Zinniker, D., DeConto, R., Huber, M., Brinkhuis, H., Shah, S.R., Leckie, R.M., Pearson, A., 2009. Global cooling during the Eocene-Oligocene climate transition. Science 323, 1187–1190. https://doi.org/10.1126/science.1166833.
Liu, H., Liao, Z.W., Zhang, H.Z., Tian, Y.K., Cheng, B., Yang, S., 2017. Stable isotope ($\delta^{13}C_{ker}$, $\delta^{13}C_{carb}$, $\delta^{18}O_{carb}$) distribution along a Cambrian outcrop section in the eastern Tarim Basin, NW China and its geochemical significance. Geosci. Front. 8 (1), 163–170. https://doi.org/10.1016/j.gsf.2016.02.004.
Liu, Z., He, Y., Jiang, Y., Wang, H., Liu, W., Bohaty, S.M., Wilson, P.A., 2018. Transient temperature asymmetry between hemispheres in the Palaeogene Atlantic Ocean. Nat. Geosci. 11, 656–660. https://doi.org/10.1038/s41561-018-0182-9.
Liu, J.G., Zheng, F.Y., Mao, F.J., Jiang, H., Li, Z.H., Li, M.S., Liu, B., Yuan, S.O., 2022. Reservoir characteristics and its controlling factors of the Paleogene Sokor1 Formation in Termit Basin, Niger. Acta Petrol. Sin. 38 (9), 2581–2594. https://doi.org/10.18654/1000-0569/2022.09.04.
Liu, Y., Wu, Z., Du, Q., Wang, M., 2024. Late Eocene tectonic-geomorphic transition and its dynamic mechanism: case study of the Beibuwan Basin, northern South China Sea. Geomorphology 467, 109458. https://doi.org/10.1016/j.geomorph.2024.109458.
López-Quirós, A., Escutia, C., Etourneau, J., Rodríguez-Tovare, F.J., Roignant, S., Lobo, F.J., Thompsong, N., Bijl, P.K., Bohoyo, F., Salzmanng, U., Evangelinosb, D., Salabarnada, A., Hoem, F.S., Sicre, M., 2021. Eocene–Oligocene paleoenvironmental changes in the South Orkney Microcontinent (Antarctica) linked to the opening of Powell Basin. Glob. Planet. Chang. 204, 103581. https://doi.org/10.1016/j.gloplacha.2021.103581.
Ma, P., Liu, Z., Huang, B., Zhao, Y., Shu, W., Li, Y., 2020. Oligocene evolution of the outermost continental margin in response to breakup and early spreading of the South China Sea. Mar. Geol. 427, 106241. https://doi.org/10.1016/j.margeo.2020.106241.
Marquez, R.T.C., Tejada, M.L.G., Suzuki, K., Peleo-Alampay, A.M., Goto, K.T., Hyun, S., Senda, R., 2017. The seawater osmium isotope record of South China Sea: implications on its its history and evolution. Mar. Geol. 394, 98–115. https://doi.org/10.1016/j.margeo.2017.07.018.
Maynard, J.B., 1992. Chemistry of modern soils as a guide to interpreting Precambrian paleosols. J. Geol. 100 (3), 279–289. https://doi.org/10.1086/629632.
McCormack, J., Nehrke, G., Jöns, N., Immenhauser, A., Kwiecien, O., 2019. Refining the interpretation of lacustrine carbonate isotope records: implications of a mineralogy-

specific Lake Van case study. Chem. Geol. 513, 167–183. https://doi.org/10.1016/j.chemgeo.2019.03.014.
Mclennan, S.M., 1989. Rare earth elements in sedimentary rocks: influence of provenance and sedimentary processes. Rev. Mineral. Geochem. 21, 169–200.
Mi, L., Zhang, G., Shen, H., Liu, Z., Guo, R., Zhong, K., Tian, J., 2008. Eocene–Lower Oligocene sedimentation characteristics of Baiyun Sag in the deep water area of Pearl River Mouth Basin. Acta Pet. Sin. 29 (1), 29–34.
Miall, A.D., 1996. The Geology of Fluvial Deposits. Sedimentary Facies, Basin Analysis, and Petroleum Geology. Springer-Verlag.
Miller, K.G., Janecek, T.R., Katz, M.E., Keil, D.J., 1987. Abyssal circulation and benthic foraminiferal changes near the Paleocene/Eocene boundary. Paleoceanography 2, 741–761. https://doi.org/10.1029/PA002i004p00741.
Miller, K.G., Browning, J.V., Aubry, M.P., Wade, B.S., Katz, M.E., Kulpecz, A.A., Wright, J.D., 2008. Eocene–Oligocene global climate and sea level changes: St. Stephens Quarry, Alabama. Geol. Soc. Am. Bull. 120 (1/2), 34–53. https://doi.org/10.1130/B26466.1.
Miller, K.G., Browning, J.V., Schmelz, W.J., Kopp, R.E., Mountain, G.S., Wright, J.D., 2020. Cenozoic Sea-level and cryospheric evolution from deep-sea geochemical and continental margin records. Sci. Adv. 6, eaaz1346. https://doi.org/10.1126/sciadv.aaz1346.
Miller, K.G., Schmelz, W.J., Browning, J.V., Rosenthal, Y., Hess, A.V., Kopp, R.E., Wright, J.D., 2024. Global mean and relative Sea-Level changes over the past 66 Myr: implications for early Eocene Ice Sheets. Earth Sci. Syst. Soc. 3, 10091. https://doi.org/10.3389/esss.2023.10091.
Naeher, S., Gilli, A., North, R.P., Hamann, Y., Schubert, C.J., 2013. Tracing bottom water oxygenation with sedimentary Mn/Fe ratios in Lake Zurich, Switzerland. Che. Geo. 352, 125–133.
National Energy Administration, China, 2012. Method of Determining Microscopically the Reflectanceof Vitrinite in Sedimentary (SY/T 5124-2012.).
National Energy Administration, China, 2018. Analytical Method for Metal Elements in Rock by ICP-AES and ICP-MS, SY/T 6404-2018.
National Energy Administration, China, 2019. Analysis Method for Carbon and Oxygen Isotope of Organic Matter and Carbonate, SY/T 5238-2019.
Nesbitt, H.W., Young, G.M., 1982. Early Proterozoic climates and plate motions inferred from major elements chemistry of lutites. Nature 299, 715–717. https://doi.org/10.1038/299715a0.
Nesbitt, H.W., Young, G.M., 1984. Prediction of some weathering trends of plutonic and volcanic rocks based on thermodynamic and kinetic considerations. Geochim. Cosmochim. Acta 48, 1523–1534. https://doi.org/10.1016/0016-7037(84)90064-2.
O'Neil, J.R., Clayton, R.N., Mayeda, T.K., 1969. Oxygen isotope fractionation in divalent metal carbonates. J. Chem. Phys. 51, 5547–5558. https://doi.org/10.1063/1.1671982.
Pagani, M., Zachos, J.C., Freeman, K.H., Tipple, B., Bohaty, S., 2005. Marked decline in atmospheric carbon dioxide concentrations during the Paleogene. Science 309, 600–603. https://doi.org/10.1126/science.1085470.
Pagani, M., Huber, M., Liu, Z.H., Bohaty, S., Henderiks, J., Sijp, W., Krishnan, S., DeConto, R., 2011. The role of carbon dioxide during the onset of Antarctic glaciation. Science 334, 1261–1264. https://doi.org/10.1126/science.1203909.
Pang, X., Ren, J., Zheng, J., Li, J., Yu, P., Liu, B., 2018. Petroleum geology controlled by extensive detachment thinning of continental margin crust: a case study of Baiyun Sag in the deep water area of northern South China Sea. Pet. Explor. Dev. 45 (1), 27–39. https://doi.org/10.1016/j.petrol.2017.10.009.
Pearson, P.N., McMillan, I.K., Wade, B.S., Jones, T.D., Coxall, H.K., Bown, P.R., Lear, C. H., 2008. Extinction and environmental change across the Eocene–Oligocene boundary in Tanzania. Geology 36 (2), 179–182. https://doi.org/10.1130/G24542A.1.
Pearson, P.N., Foster, G.L., Wade, B.S., 2009. Atmospheric carbon dioxide through the Eocene–Oligocene climate transition. Nature 461, 1110–1113. https://doi.org/10.1038/nature08421.
Pei, J., Zhao, Y., Zhou, Z., Yang, Z., Liu, X., Zheng, G., Tong, Y., Li, J., Hou, L., 2021. Impact of Cenozoic Antarctic continent-ocean configuration patterns on global climate change. J. Geom. 27 (5), 867–879. https://doi.org/10.1680/jgeomech.19.a5025.
Peng, G.R., Guo, J., Jiang, F.J., Jiang, D., Wu, Y., Chen, Z., Song, Z., Gao, Z., Zhang, Y., 2023. Geochemical characteristics of source rocks and oil source correlation in Kaiping sag, Pearl River Mouth Basin. Acta Petrol. Sin. 44 (10), 1624–1636. https://doi.org/10.7623/syxb202310004.
Piller, W.E., Harzhauser, M., Kranner, M., Mandic, O., Mohtat, T., Daneshian, J., 2024. The Tethyan Seaway during the early to middle Miocene—New data and a review. Gondwana Res. 135, 57–74. https://doi.org/10.1016/j.gr.2023.08.014.
Pound, M.J., Salzmann, U., 2017. Heterogeneity in global vegetation and terrestrial climate change during the late Eocene to early Oligocene transition. Sci. Rep. 7, 43386. https://doi.org/10.1038/srep43386.
Premoli Silva, I., Jenkins, D.G., 1993. Decision on the Eocene–Oligocene boundary stratotype. Episodes 16, 379–382.
Qin, G., 1996. Application of micropaleontology to the sequence stratigraphic studies of late Cenozoic in the Zhujiang River Mouth Basin. Mar. Geol. Quat. Geol. 16 (4), 1–18.
Rae, J.W.B., Zhang, Y.G., Liu, X., Foster, G.L., Stoll, H.M., Whiteford, R.D.M., 2021. Atmospheric CO_2 over the Past 66 Million Years from Marine Archives. Annual Rev. Earth Plane. Sci. 49, 609–641.
Raymo, M.E., Ruddiman, W.F., 1992. Tectonic forcing of late Cenozoic climate. Nature 359, 117–122. https://doi.org/10.1038/359117a0.
Retallack, G.J., 2000. Depth to pedogenic carbonate horizon as a paleo-precipitation indicator? Comment. Geol. 28, 572. https://doi.org/10.1130/G28060.1.
Retallack, G.J., 2001. Cenozoic expansion of grasslands and climatic cooling. J. Geol. 109, 407–426. https://doi.org/10.1086/320791.
Rieu, R., Allen, P.A., Plötze, M., Pettke, T., 2007. Climatic cycles during a Neoproterozoic "snowball" glacial epoch. Geology 35 (4), 299–302. https://doi.org/10.1130/G23400A.1.
Rohling, E.J., Foster, G.L., Gernon, T.M., Grant, K.M., Heslop, D., Hibbert, F.D., Roberts, A.P., Yu, J., 2022. Comparison and Synthesis of sea-level and deep-sea temperature variations over the past 40 million years. Rev. Geophys. 60, e2022RG000775. https://doi.org/10.1029/2022RG000775.
Ru, K., 1988. The development of superimposed basin on the northern margin of the South China Sea and its tectonic significance. Oil Gas Geol. 9 (1), 22–31.
Ruffell, A., Worden, R., 2000. Palaeoclimate analysis using spectral gamma-ray data from the Aptian (cretaceous) of southern England and southern France: Palaeogeogr. Palaeoclimatol. Palaeoecol. 155 (3), 265–283. https://doi.org/10.1016/S0031-0182(99)00119-4.
Rull, V., 2023. Eocene/Oligocene Global Disruption and the Revolution of Caribbean Mangroves. Perspectives in Plant Ecology, Evolution and Systematics.
Sahy, D., Condon, D.J., Terry Jr., D.O., Fischer, A.U., Kuiper, K.F., 2015. Synchronizing terrestrial and marine records of environmental change across the Eocene–Oligocene transition. Earth Planet. Sci. Lett. 427, 171–182. https://doi.org/10.1016/j.epsl.2015.07.002.
Savva, D., Pubellier, M., Franke, D., Chamot-Rooke, N., Meresse, F., Steuer, S., Auxietre, J.L., 2014. Different expressions of rifting on the South China Sea margins. Mar. Petrol. Geol. 58, 579–598. https://doi.org/10.1016/j.marpetgeo.2014.05.023.
Scher, Howie D., Whittaker, Joanne M., Williams, Simon E., Latimer, Jennifer C., Kordesch, Wendy E.C., Delaney, Margaret L., 2015. Onset of Antarctic circumpolar current 30 million years ago as Tasmanian Gateway aligned with westerlies. Nat. Geosci. 8, 776–780. https://doi.org/10.1038/ngeo2527.
Schulz, H.M., Bechtel, A., Sachsenhofer, R.F., 2005. The birth of the Paratethys during the early Oligocene: from Tethys to an ancient Black Sea analogue? Glob. Planet. Chang. 49, 163–176. https://doi.org/10.1016/j.gloplacha.2005.07.001.
Shackleton, N., Kennett, J.P., 1975. Paleotemperature history of the cenozoic and the initiation of antarctic glaciation: oxygen and carbon isotope analyses in DSDP Sites 277, 279 and 281. Geology 3, 655–660. https://doi.org/10.1029/GS03207.
Shao, L., Meng, A., Li, Q., Qiao, P., Cui, Y., Cao, L., Chen, S., 2017. Detrital zircon ages and elemental characteristics of the Eocene sequence in IODP Hole U1435A: implications for rifting and environmental changes before the opening of the South China Sea. Mar. Geol. 394, 39–51. https://doi.org/10.1016/j.margeo.2017.07.001.
Sheldon, N.D., Retallack, G.J., Tanaka, S., 2002. Geochemical climofunctions from North American soils and application to paleosols across the Eocene–Oligocene boundary in Oregon. J. Geol. 110, 687–696. https://doi.org/10.1086/342865.
Sluiter, I.R.K., Holdgate, G.R., Reichgelt, T., Greenwood, D.R., Kershaw, A.P., Schultz, N. L., 2022. A new perspective on late Eocene and Oligocene vegetation and paleoclimates of South-eastern Australia. Palaeogeogr. Palaeoclimatol. Palaeoecol. 596, 110985. https://doi.org/10.1016/j.palaeo.2022.110985.
Speijer, R.P., Pälike, H., Hollis, C.J., et al., 2020. Chapter 28 - the Paleogene Period. Geologic Time Scale 2020. https://doi.org/10.1016/B978-0-12-824360-2.00028-0.
Stach, E., Mackowsky, M., Teichmüller, M., Taylor, G., Chandra, D., Teichmüller, R., 1982. Stach's Textbook of Coal Petrology. Gebruder Borntraeger, Berlin.
Sun, J.M., Windley, B.F., 2015. Onset of aridification by 34 Ma across the Eocene–Oligocene transition in Central Asia. Geology 43, 1015–1018. https://doi.org/10.1130/G37165.1.
Sun, J., Ni, X., Bi, S., Wu, W., Ye, J., Meng, J., Windley, B.F., 2014. Synchronous turnover of flora, fauna, and climate at the Eocene–Oligocene Boundary in Asia. Sci. Rep. 4, 7463. https://doi.org/10.1038/srep07463.
Sun, J.M., Windley, B.F., Zhang, Z., 2016. Diachronous seawater retreat from the southwestern margin of the Tarim Basin in the late Eocene. J. Asian Earth Sci. 116, 222–231. https://doi.org/10.1016/j.jseaes.2016.03.008.
Sun, J.M., Zhang, Z.L., Cao, M.M., Windley, B.F., Tian, S.C., Sha, J.G., Abdulov, S., Gadoev, M., Oimahmadov, I., 2020. Timing of seawater retreat from proto-Paratethys, sedimentary provenance, and tectonic rotations in the late Eocene–early Oligocene in the Tajik Basin, Central Asia. Palaeogeogr. Palaeoclimatol. Palaeoecol. 545, 109657. https://doi.org/10.1016/j.palaeo.2020.109657.
Sun, J., Liu, W., Guo, Z., Qi, L., Zhang, Z., 2022. Enhanced aridification across the Eocene/Oligocene transition evidenced by geochemical record in the Tajik Basin, Central Asia. Glob. Planet. Chang. 211, 103789. https://doi.org/10.1016/j.gloplacha.2022.103789.
Talbot, M.R., Kelts, K., 1990. Paleolimnological Signatures From Carbon and Oxygen Isotopic Ratios in Carbonates, from Organic Carbon-Rich Lacustrine Sediments: Chapter 6 AAPG Mem, pp. 99–112.
Tang, H., Cui, H., Li, S., Spicer, R.A., Li, S., Su, T., Zhou, Z.K., Witkowski, C.R., Lauretano, V., Wei, G., 2024. Orbital-paced silicate weathering intensity and climate evolution across the Eocene–Oligocene transition in the southeastern margin of the Tibetan Plateau. Glob. Planet. Chang. 234, 104388. https://doi.org/10.1016/j.gloplacha.2024.104388.
Taylor, B., Hayes, D.E., 1983. Origin and history of the South China Sea basin. In: Hayes, D.E. (Ed.), The Tectonic and Geologic Evolution of Southeast Asian Seas and Islands, Part 2 American Geophysical Union, Geophysical Monograph, vol. 27, pp. 23–56. https://doi.org/10.1029/GM027p0023.
Tigchelaar, M., von der Heydt, A.S., Dijkstra, H.A., 2011. A new mechanism for the two step $\delta^{18}O$ signal at the Eocene–Oligocene boundary. Clim. Past 7 (1), 235–247.
Tribovillard, N., Algeo, T.J., Lyons, T., Riboulleau, A., 2006. Trace metals as paleoredox and paleoductivity proxies: an update. Chem. Geol. 232, 1–32. https://doi.org/10.1016/j.chemgeo.2006.02.012.

Villa, G., Fioroni, C., Persico, D., Roberts, A.P., Florindo, F., 2014. Middle eocene to late oligocene Antarctic glaciation/deglaciation and Southern Ocean productivity. Paleoceanography 29, 223–237. https://doi.org/10.1002/palo.20030.

Vonhof, H.B., Smit, J., Brinkhuis, H., Montanari, A., Nederbragt, A.J., 2000. Global cooling accelerated by early late Eocene impacts? Geology 28 (8), 687–690. https://doi.org/10.1130/G28080.1.

Wang, W., Yang, X., Bidgoli, T.S., Ye, J., 2019. Detrital zircon geochronology reveals source-to-sink relationships in the Pearl River Mouth Basin, China. Sediment. Geol. 388, 81–98.

Wang, D., Roberts, A.P., Rohling, E.J., Yao, W., Zhong, Y., Yao, Z., Lu, Y., Liu, Q., 2023a. Equatorial Pacific dust fertilization and source weathering influences on Eocene to Miocene global CO_2 decline. Commun. Earth Environ. 4, 37. https://doi.org/10.1038/s43247-023-00702-y.

Wang, W., Tian, L., Castillo, P.R., Wu, T., Dong, Y., Liu, H., Chen, L., 2023b. Petrogenesis of high-alumina basalts: implications for magmatic processes associated with the opening of the South China Sea. Chem. Geol. 636, 121641. https://doi.org/10.1016/j.chemgeo.2023.121641.

Wei, W., Algeo, T.J., 2020. Elemental proxies for paleosalinity analysis of ancient shales and mudrocks. Geochim. Cosmochim. Acta 287, 341–366.

Westerhold, T., Röhl, U., Pälike, H., Wilkens, R., Wilson, P.A., Acton, G., 2014. Orbitally tuned timescale and astronomical forcing in the middle Eocene to early Oligocene. Clim. Past 10, 955–973.

Westerhold, T., Marwan, N., Drury, A.J., et al., 2020. An astronomically dated record of Earth' s climate and its predictability over the last 66 million years. Science 369 (6509), 1383–1387. https://doi.org/10.1126/science.aba6853.

Wu, J., Suppe, J., 2018. Proto-South China Sea Plate tectonics using subducted slab constraints from tomography. J. Earth Sci. 29, 1304–1318. https://doi.org/10.1007/s12583-017-0813-x.

Wu, G., Qin, J., Mao, S., 2003. Oligocene marine pollen records in the South China Sea. Chin. Sci. Bull. 17, 1868–1871.

Wu, J., Suppe, J., Lu, R.Q., Kanda, R., 2016. Philippine Sea and East Asian Plate tectonics since 52 Ma constrained by new subducted slab reconstruction methods. J. Geophys. Res. Solid Earth 121 (6), 4670–4741. https://doi.org/10.13039/501100006477.

Wu, Y., Jiang, F., Xu, Y., Guo, J., Zheng, X., Chen, D., Xing, H., Xu, T., Hu, T., Huang, R., Zhu, Q., 2024. Doubthouse climate influences on the carbon cycle and organic matter enrichment in lacustrine basins: astrochronological and paleontological perspectives. J. Asian Earth Sci. 106155.

Wu, Y., Jiang, F., Xu, Y., Guo, J., Xu, T., Hu, T., Shen, W., Zheng, X., Chen, D., Jiang, Q., Yu, S., 2025. Middle eocene climatic optimum drove palaeoenvironmental fluctuations and organic matter enrichment in lacustrine facies of the Bohai Bay Basin, China. Palaeogeogr. Palaeoclimatol. Palaeoecol. 659, 112665. https://doi.org/10.1016/j.palaeo.2024.112665.

Xia, G., Mansour, A., Shi, Z., Hao, X., Ahmed, M.S., Radwan, A.E., Machaniec, E., 2024. Cold climatic snaps during the Eocene–Oligocene transition in the central Tibetan Plateau: implications for ice-induced sedimentary structures and isotope geochemistry. Palaeogeogr. Palaeoclimatol. Palaeoecol. 637, 112010. https://doi.org/10.1016/j.palaeo.2023.112010.

Zachos, J.C., Kump, L.R., 2005. Carbon cycle feedbacks and the initiation of Antarctic glaciation in the earliest Oligocene. Glob. Planet. Chang. 47, 51–66. https://doi.org/10.1016/j.gloplacha.2005.04.006.

Zachos, J.C., Breza, J.R., Wise, S.W., 1992. Early Oligocene ice-sheet sedimentological expansion on Antarctica: stable isotope and evidence from Kerguelen Plateau, southern Indian Ocean. Geology 20 (6), 569–573. https://doi.org/10.1130/G20060.1.

Zachos, J., Pagani, M., Sloan, L., Thomas, E., Billups, K., 2001. Trends, rhythms, and aberrations in global climate 65 Ma to present. Science 292, 686–693. https://doi.org/10.1126/science.1059412.

Zachos, J.C., Dickens, G.R., Zeebe, R.E., 2008. An early Cenozoic perspective on greenhouse warming and carbon-cycle dynamics. Nature 451, 279–283. https://doi.org/10.1038/nature06498.

Zeng, Y., Chen, J.A., Zhu, Z.J., 2011. Advance and prospective of Rb/Sr ratios in lake sediments as an index of paleoclimate/paleoenvironment. Adv. Earth Science 26 (8), 805–810. https://doi.org/10.11867/j.issn.1001-8166.2011.08.0805.

Zhang, Z.S., Nisancioglu, K.H., Flatpy, F., Bentsen, M., Bethke, I., Wang, H., 2011. Tropical seaways played a more important role than high latitude seaways in Cenozoic cooling. Clim. Past 7 (3), 801–813.

Zhang, G., Jia, Q., Wang, W., Wang, P., Zhao, Q., Sun, X., Xie, X., Zhao, Z., Tang, W., 2018. On tectonic framework and evolution of the South China Sea. Chinese J. Geophys. (in Chinese) 61 (10), 4194–4215.

Zhang, L.L., Shu, L.F., Feng, X., et al., 2020. Further discussion on the age assignment of enping formation in the Pearl River Mouth basin. China Offshore Oil Gas 32 (5), 9–18. https://doi.org/10.11935/i.issn.1673-506.2020.05.002.